3. GLOBAL OCEANS

a. *Overview*—G. C. Johnson

The transition from a strong El Niño in late 2015 to a weak La Niña by late 2016 included strengthening westward zonal surface current anomalies along the equator, which in turn contributed to sea level and upper ocean heat content rising in the western tropical Pacific north of the equator, and falling in the eastern equatorial Pacific. With resumed upwelling in the eastern equatorial Pacific, sea surface temperatures (SSTs) there cooled, outgassing of CO_2 increased, chlorophyll-a levels were high, and local heat flux from atmosphere to ocean increased. Surface salinity freshened in the western equatorial Pacific, under increased precipitation.

El Niño events modulate the rise in global mean SST and ocean heat content (OHC), with warming rates increasing as El Niños wax, and decreasing as they wane. Hence, global SST in 2016 barely broke its 2015 record high, and global OHC from 0–2000 m fell somewhat in 2016 from its 2015 record high. As a result, sea level also rose more slowly in 2016 than in 2015. To summarize in haiku form:

Large El Niño wanes,
east Pacific tropics cool,
seas shed heat, slow rise.

SST, OHC, and sea level were all anomalously low around the centers of the extratropical North and South Pacific, and generally high elsewhere, consistent with the continued warm phase of the Pacific decadal oscillation that has held since 2014. Strong winds with anomalously high heat and CO_2 loss from the ocean were observed around the eastern sides of these extratropical cold anomalies in both hemispheres in 2016.

North Atlantic SSTs southeast of Greenland rose from 2015 to 2016, but remained below average, as they have for three years now, again with anomalously low OHC and sea level, low sea surface salinity (SSS), low chlorophyll-a, and anomalous heat flux into the ocean. (Arctic Ocean SST and sea ice are discussed in detail in Chapter 5.) Western North Atlantic subtropical SSTs remained anomalously high in 2016, again with high OHC and sea level along the east coast of North America. In climate models this North Atlantic SST pattern is associated with a reduction in the Atlantic meridional overturning circulation. The coastal warming also impacts ecosystems, which have shifted north or deeper in response.

In the Indian Ocean, SSTs fell in 2016 from record-high 2015 levels, although still high compared to the long-term average. OHC and sea level rose north of about 10°S and fell south of there, resulting in anomalous eastward zonal surface currents near 10°S. Surface salinities in 2016 were generally anomalously low in the eastern Indian Ocean and high in the western Indian Ocean, a pattern that has held since the 2010/11 La Niña, also consistent with the tendency of precipitation minus evaporation from 2015 to 2016.

The rate of ocean uptake of carbon from the atmosphere has continued to generally risen along with atmospheric CO_2 concentrations, hence the ocean has acidify. The 1993–2016 trends in OHC reflect statistically significant warming in the Southern Hemisphere, mostly north of the Antarctic Circumpolar Current. (Southern Ocean conditions and sea ice are discussed in detail in Chapter 6.)

b. *Sea surface temperatures*—B. Huang, J. Kennedy, Y. Xue, and H.-M. Zhang

Sea surface temperature is a key variable in climate assessment and monitoring and is a major source of climate predictability at seasonal to interannual time scales. In 2016, SST in the tropical Pacific evolved from strong El Niño conditions in late 2015/early 2016 toward neutral or slightly-colder-than-average conditions (with the reference to the 1981–2010 climatology) by fall 2016. The 2015/16 El Niño event is one of the strongest three such events since at least 1950 (Huang et al. 2016a; Xue and Kumar 2016). Despite the weakening 2015/16 El Niño event in 2016, the global-average SST in 2016 broke the record set in 2015 by a narrow margin.

The Extended Reconstruction SST version 4 (ERSSTv4; Huang et al. 2015) is used in this report to assess SST and its change in the global oceans. ERSSTv4 is a monthly 2° × 2° SST product from 1854 to present based on in situ observations. ERSSTv4 is compared with the Daily Optimum Interpolation SST (DOISST; Reynolds et al. 2007) and U.K. Met Office Hadley Centre SST version 3 (HadSST.3.1.0.0; Kennedy et al. 2011a,b). DOISST is a daily 0.25° × 0.25° SST product for the modern satellite era from September 1981 to present using both in situ and satellite observations. HadSST.3.1.0.0 is a monthly 5° × 5° SST product from 1850 to present using in situ observations. All datasets are averaged to monthly 2° × 2° grids for comparison purposes.

Annually averaged SST anomaly (SSTA; relative to 1981–2010 climatology) in 2016 exceeded +0.5°C over much of the tropical oceans and exceeded +1°C near the Gulf of Alaska and the Gulf Stream (Fig. 3.1a). Higher SSTAs were partly associated with the 2015/16 El Niño event (Xue et al. 2016; L'Heureux
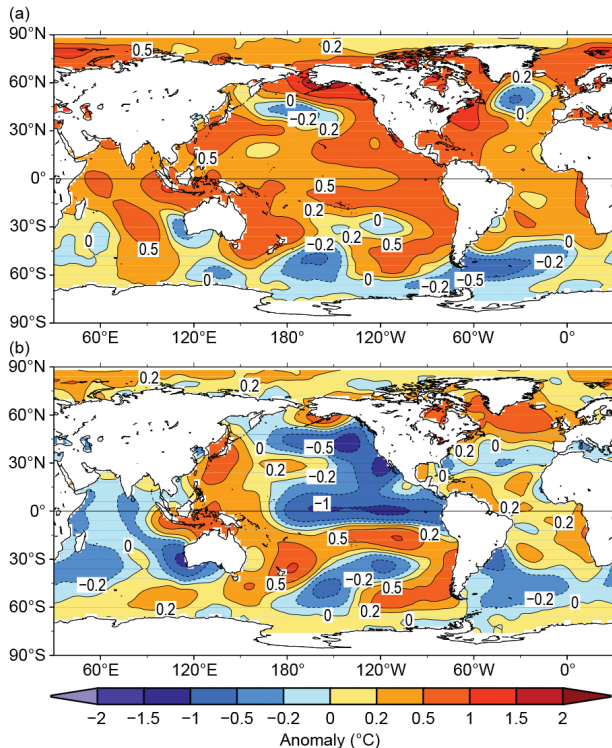
FIG. 3.1. (a) Annually averaged SSTA of ERSSTv4 in 2016 and (b) difference of annually averaged SSTAs between 2016 and 2015. SSTAs (°C) are relative to 1981–2010 climatology.

et al. 2017), which peaked in November 2015, weakened, and became neutral after June 2016. In contrast, SSTA was slightly lower than average in the Southern Ocean south of 40°S between 120°E and 0°, the northern North Atlantic south of Greenland near 50°N, and the central North Pacific near 40°N. Globally averaged SSTA in 2016 was 0.378 (±0.055) °C, marginally higher (0.013°C) than the record of 0.365 (±0.055) °C set in 2015.

In comparison with 2015, SST in 2016 was 0.2°–0.5°C higher in the western North Pacific, Indo-Pacific maritime region, western South Pacific, subtropical South Pacific along latitudes of 10°–30°N, eastern South Pacific, Atlantic between 30°S and 30°N, northern North Atlantic north of 40°N, and the Arctic (Fig. 3.1b). However, SST in 2016 was 0.5°–1.0°C lower in the central to eastern tropical Pacific and eastern subtropical North Pacific, and was approximately 0.2°C lower in the central South Pacific/Southern Ocean, South Atlantic south of 30°S, and most of the Indian Ocean.

Cooling in the tropical Pacific in 2016 relative to 2015 was clearly associated with

the weakening 2015/16 El Niño event (Figs. 3.2a–d). SSTAs in the tropical Pacific were more than two standard deviations (2σ; derived from ERSSTv4 in 1981–2010) above average in DJF 2015/16 (hereafter DJF), weakened in MAM, and became negative in JJA and SON.

In the North Pacific north of 30°N, SSTA was both 1–2 σ higher than average in the east and 1–2 σ lower in the central-west in both DJF and MAM. The low SSTA in the central-west diminished in JJA and reemerged in SON. The high SSTA is consistent with the positive phase of the Pacific decadal oscillation (PDO) in DJF and MAM, and is also consistent with El Niño conditions in the tropical Pacific.

In the western South Pacific east of Australia, SSTA was approximately 1 σ higher in DJF, strengthened to 1–2 σ in MAM and JJA, and weakened to 1 σ in SON. In the central-eastern subtropical South Pacific, SSTA was 1–2 σ higher in DJF and MAM, which shifted eastward in JJA, and weakened to approximately 1 σ in SON.

In the Indian Ocean, SSTA was 1–2 σ higher in DJF and MAM, weakened to approximately 1 σ in JJA, and dropped to less than 1 σ in SON. SSTA values in the tropical Indian Ocean in DJF and MAM are consistent with the influence of El Niño events in the region. A transition to neutral-to-low anomalies in SON seems to be associated with a transition to La Niña conditions then.
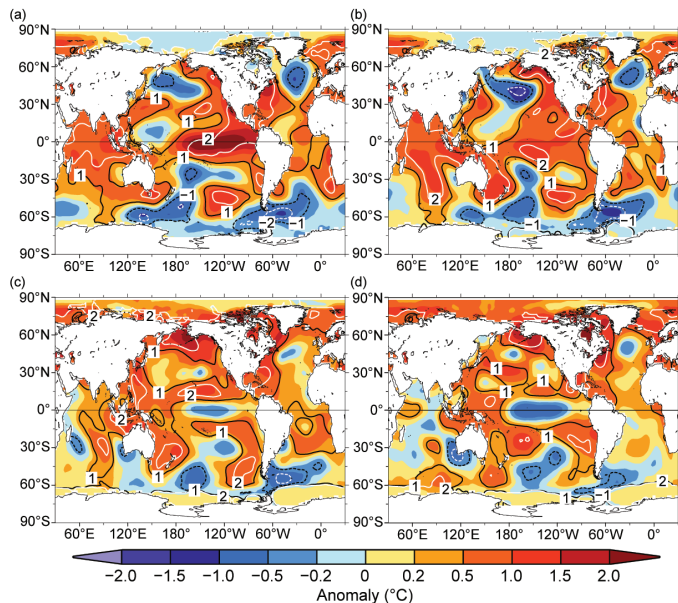

FIG. 3.2. Seasonal averaged SSTAs of ERSSTv4 (°C; shading) for (a) Dec 2015–Feb 2016, (b) Mar–May 2016, (c) Jun–Aug 2016, and (d) Sep–Nov 2016. Normalized seasonal mean SSTA based on seasonal mean std. dev. over 1981–2010 indicated by contours of 2 (dashed white), −1 (dashed black), 1 (solid black), and 2 (solid white).

SSTA persisted 1–2 σ higher in the Gulf of Alaska and subtropical North Pacific in all seasons and was approximately 1 σ higher in the tropical and South Atlantic in DJF, MAM, and JJA but weakened to less than 1 σ higher in SON. In the northern North Atlantic, the cold blob south of Greenland (de Jong and de Steur 2016) weakened in the latter half of 2016. Cold anomalies in the high-latitude Southern Ocean persisted largely through 2016.

The record high SST in 2015 and 2016 indicated a continued warming of the global oceans since 1950 (Fig. 3.3a; solid white line) or earlier (Fig. 3.3b; solid white line). The global ocean SST trend for 2000–16 of +1.62 (±0.76) °C century^{-1} is higher than the longer term 1950–2016 warming trend of 1.00 (±0.11) °C century^{-1}, although trends for the two time periods do overlap within uncertainties. Further analysis indicates that SST increase for the period 2000–16 was fastest in the North Pacific (Fig. 3.3d; 2.84°C century^{-1}) and tropical Indian Ocean (Fig. 3.3e; 2.48°C century^{-1}), with lower rates in the tropical Pacific (Fig. 3.3c; 1.61°C century^{-1}), tropical Atlantic (Fig. 3.3g; 1.35°C century^{-1}), Southern (Fig. 3.3h; 1.15°C century^{-1}), and North Atlantic (Fig. 3.3f; 1.00°C century^{-1}) oceans. The SST increase for the period 1950–2016 was fastest in the tropical Indian (1.47°C century^{-1}), tropical Atlantic (1.12°C century^{-1}), and Southern (1.02°C century^{-1}) oceans; and slower in the tropical Pacific (1.00°C century^{-1}), North Atlantic (1.00°C century^{-1}), and North Pacific (0.65°C century^{-1}) oceans. The recent increase of the global mean SST (to the end of 2015) as seen in ERSSTv4 is consistent with the report by Karl et al. (2015) and corroborated by comparisons with independent and homogenous datasets (Hausfather et al. 2017).

In addition to long-term SST trends, internal SST variations can be seen in all global ocean basins, although the amplitude is typically smaller in the Southern Ocean. Variations associated with the Atlantic multidecadal oscillation (AMO) can clearly be identified (Huang et al. 2015) with warm periods from 1950 to 1955 and 1996 to 2016, and a cold period in between.

SSTA deviations of DOISST and HadSST.3.1.0.0 from ERSSTv4 are largely within 2 σ (gray shading in Fig. 3.3). ERSSTv4 2 σ is estimated from a
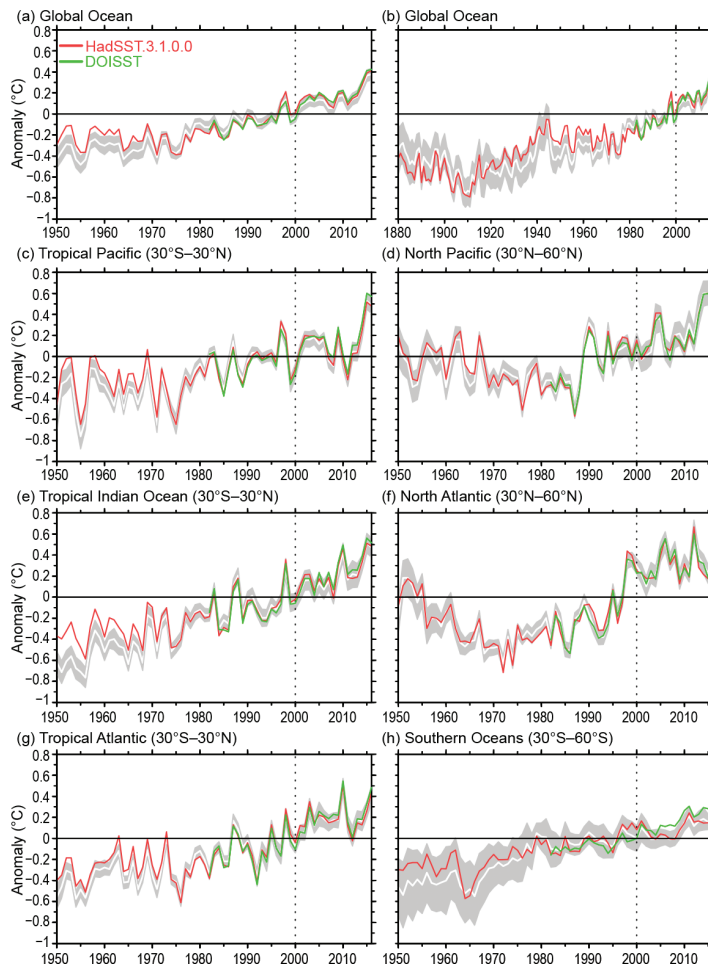

Fig. 3.3. Annually averaged SSTAs (white line) and 2σ (gray shading) of ERSSTv4, SSTAs of DOISST (green line), and SSTAs of HadSST.3.1.0.0 (red line). (a) global (1950–2016), (b) global (1880–2016), and (c) tropical Pacific, (d) North Pacific, (e) tropical Indian, (f) North Indian, (g) tropical Atlantic, and (h) Southern Oceans (1950–2016). The year 2000 is indicated by a vertical dotted line.

1000-member ensemble analysis (Huang et al. 2016b) and centered on SSTA of ERSSTv4. However, SSTAs are slightly higher in the 1950s–70s and 1920s–30s in HadSST.3.1.0.0 than in ERSSTv4. SSTAs are also slightly higher in the 2000s–10s in HadSST.3.1.0.0 and DOISST than in ERSSTv4. These SSTA differences have been mostly attributed to the differences in ship bias corrections in different products (Huang et al. 2015). Therefore, SST trends are slightly weaker in HadSST.3.1.0.0 in both 1950–2016 and 2000–16. In contrast, SST trends are slightly higher in DOISST in 2000–16. For example, the trend of globally averaged SSTA is 1.36 (±0.91) °C century^{-1} and 1.84 (±0.77) °C century^{-1}, respectively, in HadSST.3.1.0.0 and DOISST in 2000–16, while it is 1.62 (±0.76) °C century^{-1} in ERSSTv4; from 1950 to 2016, it is 0.82 (±0.17) °C century^{-1} in HadSST.3.1.0.0 and 1.00 (±0.11) °C

century^{-1} in ERSSTv4 (Table 3.1). These trends agree within their uncertainty ranges.

c. *Ocean heat content*—
G. C. Johnson, J. M. Lyman, T. Boyer, C. M. Domingues, J. Gilson, M. Ishii, R. Killick, D. Monselesan, and S. E. Wijffels

Storage and transport of heat in the ocean are central to aspects of climate such as ENSO (Johnson and Birnbaum 2017), tropical cyclones (Goni et al. 2009), sea level rise (Leuliette 2015), variations in the global average surface warming rate (Xie et al. 2016), and melting of ice sheet outlet glaciers around Greenland (Castro de la Guardia et al. 2015) and Antarctica (Schmidtko et al. 2014). Ocean warming accounts for about 93% of the total increase in Earth's energy storage from 1971 to 2010 (Rhein et al. 2013).

Maps of annual (Fig. 3.4) upper (0–700 m) ocean heat content anomaly (OHCA) relative to a 1993–2016 baseline mean are generated from a combination of in situ ocean temperature data and satellite altimetry data following Willis et al. (2004), but using Argo (Riser et al. 2016) data downloaded in January 2017. Near-global average seasonal temperature anomalies (Fig. 3.5) vs. pressure from Argo data (Roemmich and Gilson 2009, updated) since 2004 and in situ global estimates of OHCA (Fig. 3.6) for three pressure layers from six different research groups (including the group responsible for the 2000–6000 m estimate) are also discussed.

The large decrease (Fig. 3.4b) of 0–700-m OHCA in the central and eastern equatorial Pacific from 2015 to 2016 is associated with the waning of the 2015/16 El Niño, as is the OHCA increase in the western and central Pacific just north of the equator (Johnson and Birnbaum 2017). This pattern is consistent with strong westward zonal current anomalies along the equator in 2016 (see Fig. 3.18). Despite this 2015/16 tendency, upper OHCA remains low with respect to the 1993–2016 average in the tropical western Pacific, and high in the eastern tropical Pacific (except for a narrow band along the equator) on both sides of the equator. This pattern has held since 2014 (Johnson et al. 2015a, 2016) and is reflected in sea level (see Fig. 3.16).

Outside the tropics, the eastern North and South Pacific upper OHCA generally rose from 2015 to 2016 (Fig. 3.4b), whereas it fell in regions in the central North and South Pacific. This pattern is consistent with a continued positive (since 2014) Pacific decadal oscillation (PDO; Mantua et al. 1997) and a positive interdecadal Pacific oscillation (IPO). North and

Table 3.1. Trends (°C century^{-1}) of globally averaged SSTAs of ERSSTv4. Uncertainties at 95% confidence incorporate degrees of freedom estimated from application of a first order autoregressive model to the annually averaged SST time series.

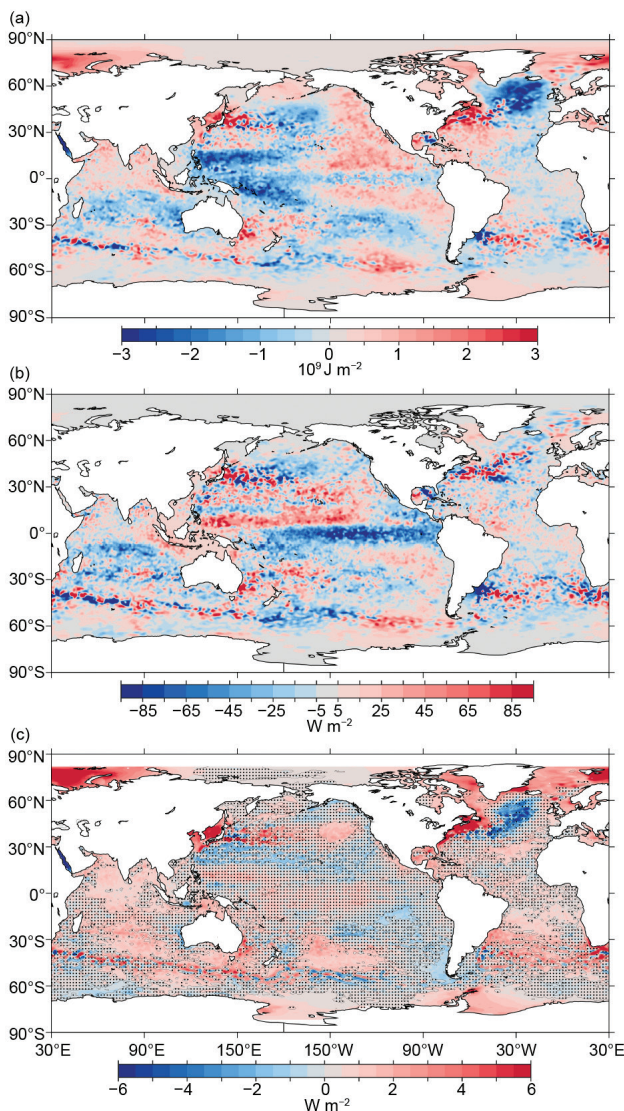|	ERSSTv4	HadSST.3.1.0.0	DOISST
2000–16	1.62±0.76	1.36±0.91	1.84±0.77
1950–2016	1.00±0.11	0.82±0.17	—

Fig. 3.4. (a) Combined satellite altimeter and in situ ocean temperature data estimate of upper (0–700 m) OHCA (× 10^9 J m^{-2}) for 2016 analyzed following Willis et al. (2004), but using an Argo monthly climatology and displayed relative to the 1993–2016 baseline. **(b)** 2016 minus 2015 combined estimates of OHCA expressed as a local surface heat flux equivalent (W m^{-2}). For (a) and (b) comparisons, note that 95 W m^{-2} applied over one year results in a 3 × 10^9 J m^{-2} change of OHCA. **(c)** Linear trend from 1993–2016 of the combined estimates of upper (0–700 m) annual OHCA (W m^{-2}). Areas with statistically insignificant trends are stippled.
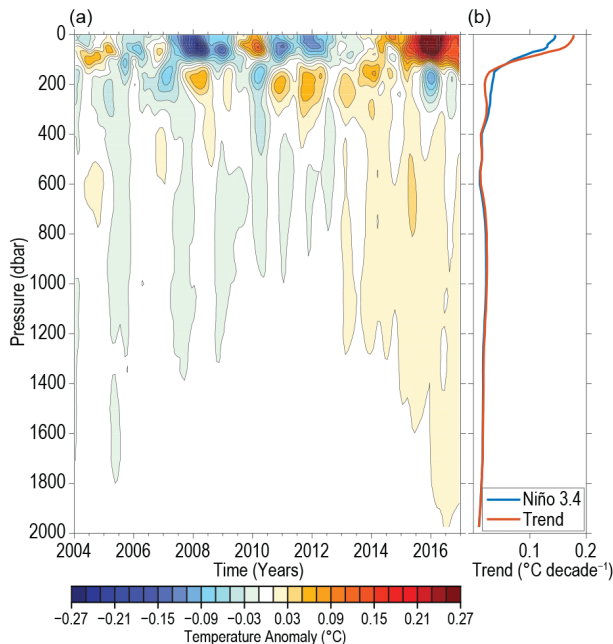
Fig. 3.5. (a) Near-global (60°S–60°N, excluding marginal seas and continental shelves) integrals of monthly temperature anomalies [°C; updated from Roemmich and Gilson (2009)] relative to record-length average monthly values, smoothed with a 5-month Hanning filter and contoured at odd 0.02°C intervals (see colorbar) vs. pressure and time. (b) Linear trend of temperature anomalies over time for the length of the record in (a) plotted vs. pressure in °C decade⁻¹ (orange line), and trend with a Niño3.4 regression removed (blue line) following Johnson and Birnbaum (2017).

South Pacific 2016 upper OHC (Fig. 3.4a), SST (see Fig. 3.1), and sea level (see Fig. 3.15a) anomalies reflect the positive PDO and IPO. A positive IPO phase may be associated with an increased rate of global average surface warming (Meehl et al. 2013) and also affects regional sea level rise rates (Zhang and Church 2012). Regions around the Kuroshio and the East Australian currents were also anomalously warm in 2016.

In the Indian Ocean there was generally warming from 2015 to 2016 north of about 10°S and around the Maritime Continent, and cooling from 10°S to 30°S (Fig. 3.4b). This pattern is consistent with increased eastward flow near 10°S in 2016 relative to 2015 (see Fig. 3.18), similar to the tendency from 2014 to 2015. Upper OHCA in the Indian Ocean remained above average in 2016 (Fig. 3.4a), except for a newly formed low band from about 10°S to 30°S, consistent with a negative phase of the Indian Ocean dipole mode index (Saji et al. 1999). The Agulhas Current remained warm in 2016.

Much of the Atlantic warmed, in both hemispheres, from 2015 to 2016 (Fig. 3.4b). However, the region around the Brazil and Malvinas/Falkland

Currents generally cooled from 2015 to 2016, leaving it cooler than average in 2016 (Fig. 3.4a). The most striking 2015 pattern in the Atlantic OHCA persisted in 2016: anomalously low subpolar North Atlantic OHCA (Fig. 3.4a) coupled with high upper OHCA offshore of much of the east coast of North America. These changes may be related to a reduction in the strength of the Atlantic meridional overturning circulation (AMOC; see Section 3h) in recent years (Saba et al. 2016).

Large-scale statistically significant (Fig. 3.4c) regional patterns in the 1993–2016 local linear trends of upper OHCA reflect a warming trend in much of the Southern Hemisphere, with the only large-scale statis-
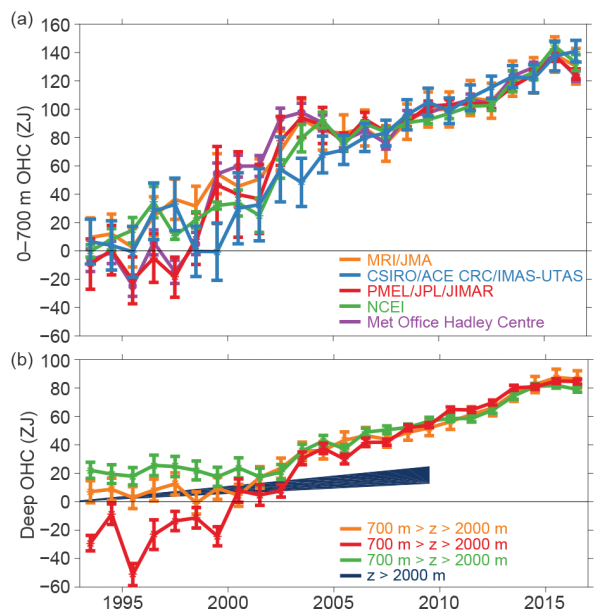

Fig. 3.6. (a) Annual average global integrals of in situ estimates of upper (0–700 m) OHCA (ZJ; 1 ZJ = 10²¹ J) for 1993–2016 with standard errors of the mean. The MRI/JMA estimate is an update and modification of Ishii and Kimoto (2009). The CSIRO/ACE CRC/IMAS-UTAS estimate is an update of Domingues et al. (2008). The PMEL/JPL/JIMAR estimate is an update and refinement of Lyman and Johnson (2014). The NCEI estimate follows Levitus et al. (2012). The Met Office Hadley Centre estimate is computed from gridded monthly temperature anomalies (relative to 1950–2016) following Palmer et al. (2007). See Johnson et al. (2014) for details on uncertainties, methods, and datasets. For comparison, all estimates have been individually offset (vertically on the plot), first to their individual 2005–16 means (the best sampled time period), and then to their collective 1993 mean. (b) Annual average global integrals of in situ estimates of intermediate (700–2000 m) OHCA for 1993–2016 with standard errors of the mean, and a long-term trend with one standard error uncertainty shown from 1992–2009 for deep and abyssal (z > 2000 m) OHCA updated (Desbruyères et al. 2016) following Purkey and Johnson (2010).

tically significant cooling trends there in the southeast tropical Pacific as well as west and south of southern Chile. This prevalence of warming in the Southern Hemisphere is consistent with 0–2000 dbar (1 dbar ~ 1 m) OHCA patterns for 2006–15 (Roemmich et al. 2015; Wijffels et al. 2016). The apparent warming trends adjacent to Antarctica are located in both in situ and altimeter data-sparse regions and are not as robust as suggested by the statistics.

There are also large-scale statistically significant warming trends (Fig. 3.4c) in the North Indian Ocean, the eastern North Pacific (around 40°N, 150°W), the eastern North Atlantic (around 25°N, 35°W), and in the Labrador and Nordic Seas, with a zonal band of statistically significant cooling trend around the Tropic of Cancer across the North Pacific. In the North Atlantic, the pattern of a large amplitude and statistically significant warming trend along the North American coast coupled with a large amplitude and statistically significant interior subpolar cooling trend (Fig. 3.4c) again may be linked to reductions in AMOC strength. Statistically significant warming trends are also present near all the subtropical western boundary currents (Lix. Wu et al. 2012).

In previous years, strongest notably in 2013 (Johnson et al. 2014), there was a statistically significant cooling trend in the eastern tropical Pacific and a statistically significant warming trend in the western tropical Pacific. That pattern has been attributed to trade wind intensification (Merrifield et al. 2012) and linked to a temporary reduction in the rate of globally averaged surface temperature increase (England et al. 2014), sometimes termed the hiatus. However, weakening of the trade winds starting in 2014, asso-

ciated with an end to the hiatus (see Fig. 3.3), as well as a shift in phase of the PDO (and perhaps the IPO) and then El Niño, has resulted in a weak and statistically insignificant warming trend across much of the tropical Pacific for 1993–2016 (Fig. 3.4c).

Near-global average seasonal temperature anomalies from 2004 to 2016 (Fig. 3.5a) largely reflect ENSO redistributing heat (e.g., Roemmich and Gilson 2011) in the upper 400 dbar, with lower values in the upper 100 dbar and higher values from 100 to 400 dbar during La Niña (e.g., 2008/09), and vice versa during El Niño (e.g., 2015/16). Since the peak of El Niño near the end of 2015, mean temperatures in the upper 100 dbar have declined, while still remaining quite high relative to time-average values. Negative anomalies from 150 to 400 dbar have also abated somewhat. In addition to the ENSO signature, there is an overall warming trend (Fig. 3.5b, orange line) from 2004 to 2016 that approaches 0.18°C decade^{-1} near the surface, declining to around 0.02°C decade^{-1} by 150 dbar and remaining near that rate down to 2000 dbar. Removing a linear regression against the Niño3.4 index (e.g., Johnson and Birnbaum 2017) results in a decadal warming trend (Fig. 3.5b, blue line) closer to 0.15°C decade^{-1} near the surface, and slightly larger from about 150 to 400 dbar.

The analysis is extended back in time from the Argo period to 1993, and deeper, using historical data collected mostly from ships. Five different estimates of globally integrated in situ 0–700-m OHCA (Fig. 3.6a) all reveal a large increase since 1993, and most indicate a slight drop in 2016 from a record high OHCA value in 2015. Global OHCA integrals are modulated by ENSO, increasing faster than the long-term warm-

TABLE 3.2. Trends of ocean heat content increase (in W m^{-2} applied over the 5.1 × 10^{14} m^2 surface area of Earth) from six different research groups over three depth ranges (see Fig. 3.6 for details). For the 0–700 and 700–2000 m depth ranges, estimates cover 1993 to 2016, with 5%–95% uncertainties based on the residuals taking their temporal correlation into account when estimating degrees of freedom (Von Storch and Zwiers 1999). The 2000–6000 m depth range estimate covers 1992–2009, again with 5%–95% uncertainty.

Research Group	Global Ocean Heat Content Trends (W m^{-2})		
	0–700 m	700–2000 m	2000–6000 m
MRI/JMA	+0.34 ± 0.06	+0.28 ± 0.16	—
CSIRO/ACE/CRC/IMAS/UTAS	+0.40 ± 0.07	—	—
PMEL/JPL/JIMAR	+0.42 ± 0.17	+0.31 ± 0.03	—
NCEI	+0.37 ± 0.07	+0.24 ± 0.08	—
Met Office Hadley Centre	+0.40 ± 0.20	—	—
Desbruyères et al. (2016)	—	—	+0.07 ± 0.04

ing trend as El Niño waxes and slower than that trend when El Niño wanes (Johnson and Birnbaum 2017). The rapid increase in OHCA in 2015 followed by a reduction in 2016 is thus consistent with the transition from a strong El Niño in early 2016 to borderline La Niña conditions in late 2016. Net OHCA appears to plateau in 2016 from 700 to 2000 m (Fig. 3.6b). Causes of the differences among estimates are discussed in Johnson et al. (2015a). From 2000 to 6000 m (Fig. 3.6b), trends are estimated from differences between decadal surveys (Desbruyères et al. 2016).

The rate of heat gain from linear trends fit to each of the five global integral estimates of 0–700 m OHCA from 1993 through 2016 (Fig. 3.6a) range from 0.34 (±0.06) to 0.42 (±0.17) W m^{-2} applied over the surface area of Earth (Table 3.2). Linear trends from 700 to 2000 m over the same time period range from 0.24

(±0.08) to 0.31 (±0.03) W m^{-2}. All trends in the upper two layers agree within uncertainties. For 2000–6000 m, the linear trend is 0.07 (±0.04) W m^{-2} from 1992 to 2009. Summing the three layers (with their slightly different time periods), full-depth ocean heat gain rate ranges from 0.65 to 0.80 W m^{-2}.

d. Salinity—G. C. Johnson, J. Reagan, J. M. Lyman, T. Boyer, C. Schmid, and R. Locarnini

1) Introduction—G. C. Johnson and J. Reagan

Salinity patterns, both means and their variations, reflect ocean storage and transport of freshwater, a key aspect of global climate (e.g., Rhein et al. 2013). Long-term means of sea surface salinity (SSS) are largely determined by patterns of evaporation, precipitation, and river runoff (e.g., Schanze et al. 2010), modified by advection and entrainment (e.g., Yu

---

SIDEBAR 3.1: CHANGES IN THE NORTHEAST U.S. SHELF ECOSYSTEM AND FISHERIES—J. HARE

The pace of observed change in the northeast U.S. shelf ecosystem, which extends from Cape Hatteras, North Carolina, through the Gulf of Maine, is faster than in many other continental shelf ecosystems (Pershing et al. 2015). Future change in the northeast U.S. shelf ecosystem also is projected to be greater than in many other portions of the world's oceans (Saba et al. 2016). Temperatures have risen ~1.5°C in this region since 1995 (Fig. SB3.1). Some of this temperature rise is attributable to long-term climate change and some of it is attributable to natural variability related to the Atlantic multidecadal oscillation. The region is also a "hotspot" for sea level rise: increases in the rates of sea level rise are ~3–4 times higher in this region compared to the global average (Sallenger et al. 2012). There are also changes in the Gulf Stream, with increased variability in the Gulf Stream path north of Cape Hatteras (Andres 2016) and recently observed direct interactions with the northeast U.S. shelf (Gawarkiewicz et al. 2012).

The northeast U.S. shelf ecosystem supports a wide array of living marine resources, from Atlantic sea scallops, one of the most valuable, to the North Atlantic right whale, one of the most endangered. All of these resources—fish, invertebrates, marine mammals, sea turtles, plants, habitats, and other ecosystem components—are being impacted by changing ocean and climate conditions in the region. The productivity of some species has been linked to temperature, with some species exhibiting decreased productivity related to warming (e.g., Atlantic cod, Fogarty et al. 2008; winter flounder, R. Bell et al. 2014) and other species exhibiting increased productivity (e.g., Atlantic croaker, Hare et al. 2010). Still other species have shown no change in productivity during the recent period of
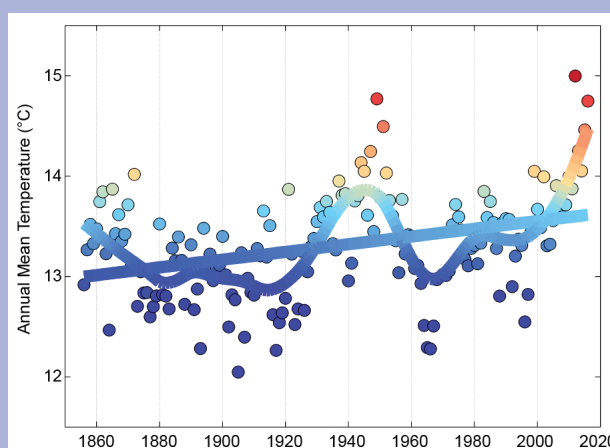

Fig. SB3.1. Mean annual temperature (°C, colors) on the northeast U.S. shelf ecosystem (36–46°N, 76–66°W) derived from the ERSSTv4 dataset (www.esrl.noaa.gov /psd/data/gridded/data.noaa.ersst.v4.html). Long-term change is estimated with a linear regression (straight line) and multidecadal variability is estimated with a loess smoother. As depicted, the temperatures, as indicated on the y-axis, transition from dark blue (lowest) to red (highest).

warming (e.g., summer flounder, R. Bell et al. 2014). This range of responses suggests that some species in the region will be negatively impacted by changes in ocean and climate conditions and other species will be positively impacted.

Changes in marine species distributions have been widely documented in the northeast U.S. shelf ecosystem. Long-term bottom trawl surveys provide an important data source for

documenting changes in distribution. The population center of many species in the southern part of the ecosystem has moved northeastward (Kleisner et al. 2016). In the northern part of the ecosystem, the population center of many species has moved southwestward. These sub-ecosystem differences are related to the complexity of the geology and oceanography in the ecosystem. The southern part of the ecosystem is a typical broad continental shelf; warming waters result in the thermal habitat moving poleward and into deeper water. The northern part of the ecosystem, the Gulf of Maine, is bathymetrically complex with deep basins, banks, and channels. The coolest water is observed in the deeper southwestern basins, and cold-water species appear to be moving into this area. These sub-ecosystem differences in distribution changes indicate the importance of physical characteristics of an ecosystem in influencing the response of species to changing ocean and climate conditions. Similar changes in distribution were observed in the late 1940s during the last warm period (Fig. SB3.1; Taylor et al. 1957; Friedland and Hare 2007).

Fisheries are also changing in the ecosystem. Fishery landings of some species are moving northward as the species themselves move northward (Pinsky and Fogarty 2012). As an example, lobster landings have shifted from Connecticut, New York, and New Jersey to Maine, partly as a result of warming temperatures and decreasing productivity in the south and increasing productivity in the north. This change in landings has greatly diminished the lobster fishery in southern New

England and resulted in a boom in Maine (Steneck and Wahle 2013). New fisheries are also developing in the region, including blueline tilefish and chub mackerel, species that historically occurred south of Cape Hatteras. A number of species are being captured by both commercial and recreational fisheries in new, predominantly more northern areas. There is also concern about the impact of ocean acidification on the region's fisheries. Laboratory and modeling studies have shown the potential for negative impacts on populations and fisheries (Talmage and Gobler 2010; Fay et al. 2017) but effects have yet to be attributed to observed changes in the region's living marine resources.

Changes in population productivity, population distribution, and fishing patterns are challenging some long-held spatial management strategies, including fixed spatial allocation of allowable catch and regional management, with species moving into new regions. These changes are also challenging the collection of fisheries data in the region. In the coming years, developing strategies to provide scientific advice for assessing and managing living marine resources in the face of changing ocean and climate conditions is going to present a major challenge to the stewardship of the nation's ocean resources and their habitat (Morrison and Termini 2016). To meet these challenges, NOAA Fisheries released a Fisheries Climate Science Strategy (Link et al. 2015), and a Regional Action Plan has been developed for the northeast U.S. shelf ecosystem (Hare et al. 2016).

2011). In some high latitude regions, sea ice formation, advection, and melt (e.g., Petty et al. 2014) can also influence SSS. Hence, relatively salty surface waters are observed in the subtropics where evaporation dominates, and fresher waters under the intertropical convergence zones (ITCZs) and in subpolar regions where precipitation dominates. Below the surface, fresher subpolar waters slide along isopycnals to intermediate depths and spread underneath saltier subtropical waters, which are in turn capped at low latitudes by fresher tropical waters (e.g., Skliris et al. 2014). Salinity changes in these layers can quantify the increase of the hydrological cycle associated with global warming over recent decades (Skliris et al. 2014). Below these layers lies salty North Atlantic Deep Water, formed mostly by open ocean convection, with salinity varying over decades (e.g., Yashayaev and Loder 2016). Fresher and colder Antarctic Bottom Waters, formed mostly in proximity to ice shelves, fill the abyss of

much of the ocean (Johnson 2008) and have been freshening in recent decades (e.g., Purkey and Johnson 2013). Salinity changes also have an effect on sea level (e.g., Durack et al. 2014) and the thermohaline circulation (e.g., Liu et al. 2017).

To investigate interannual changes of subsurface salinity, all available salinity profile data are quality controlled following Boyer et al. (2013) and then used to derive 1° monthly mean gridded salinity anomalies relative to a long-term monthly mean for years 1955–2012 (World Ocean Atlas 2013 version 2; WOA13v2; Zweng et al. 2013) at standard depths from the surface to 2000 m (Boyer et al. 2012). In recent years, the largest source of salinity profiles is the profiling floats of the Argo program (Riser et al. 2016). These data are a mix of real-time (preliminary) and delayed-mode (scientific quality controlled) observations. Hence, the estimates presented here could change after all data have been subjected to scientific

quality control. The SSS analysis relies on Argo data downloaded in January 2017, with annual maps generated following Johnson and Lyman (2012) as well as monthly maps of bulk (as opposed to skin) SSS data from BASS (Xie et al. 2014). BASS blends in situ SSS data with data from the *Aquarius* (Le Vine et al. 2014; mission ended in June 2015) and SMOS (Soil Moisture and Ocean Salinity; Font et al. 2013) satellite missions. BASS maps can be biased fresh around land (including islands) and should be compared carefully with in situ data-based maps at high latitudes before trusting features there. Despite the lower accuracies of satellite data relative to Argo data, their higher spatial and temporal sampling allows higher spatial and temporal resolution maps than are possible using in situ data alone. Salinity is measured as a dimensionless quantity and reported on the 1978 Practical Salinity Scale, or PSS-78 (Fofonoff and Lewis 1979).

2) Sea surface salinity—G. C. Johnson and J. M. Lyman

The 2016 SSS anomalies (Fig. 3.7a, colors) reveal some large-scale patterns that largely held from 2004 to 2015 (e.g., Johnson et al. 2016, and previous *State of the Climate* reports). Regions around the subtropical salinity maxima are generally salty with respect to WOA13v2. While less clear in 2016 than in previous years, some high-latitude, low-salinity regions are slightly fresher overall than WOA13v2, primarily in portions of the subpolar gyres of the North Pacific and North Atlantic. These multiyear patterns are consistent with an increase in the hydrological cycle (e.g., more evaporation in drier locations and more precipitation in rainy areas) over the ocean, as expected in a warming climate (Rhein et al. 2013). The large, relatively fresh patch in 2016 in the eastern Indian Ocean north of 30°S has been present back to 2011 (Johnson and Lyman 2012). It originally resulted from high precipitation owing to the interaction of the strong 2010–12 La Niña with other climate patterns (Fasullo et al. 2013).

Sea surface salinity changes from 2015 to 2016 (Fig. 3.7b, colors) strongly reflect 2016 anomalies in evaporation minus precipitation (see Fig. 3.12). Advection by anomalous ocean currents (see Fig. 3.18) also plays a role in SSS changes. Prominent large-scale SSS changes from 2015 to 2016 reflect salinification on either side of Central America, east of the Philippines, and in the Labrador Sea (Fig. 3.7b). Freshening during this time period is prominent around the Maritime Continent, in the Bay of Bengal, in the northeast tropical Pacific fresh pool, in portions of the subtropical and subpolar North Pacific, and east of Greenland. The tropical Pacific changes are likely owing to the

transition from the strong 2015/16 El Niño to weak La Niña conditions later in 2016.

Seasonal variations of SSS anomalies in 2016 (Fig. 3.8) from BASS (Xie et al. 2014) show that fresh anomalies in the eastern Indian Ocean peak in March–May. Fresh anomalies increased in the center of the subpolar North Pacific over the course of the year, with salty anomalies in the eastern North Pacific peaking in June–August. In the equatorial Pacific
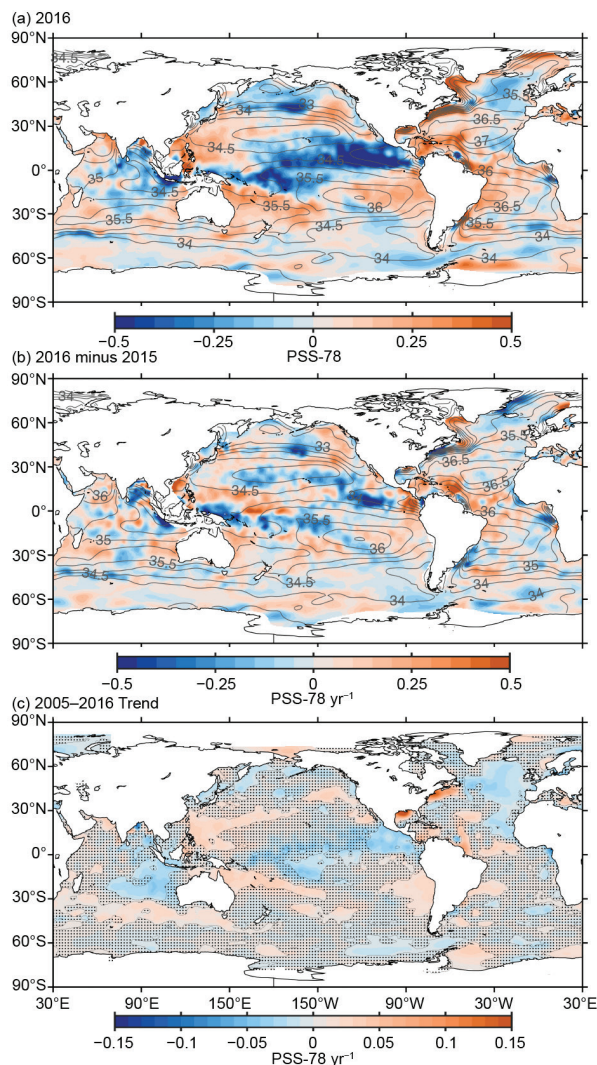

Fig. 3.7. (a) Map of the 2016 annual surface salinity anomaly (colors, PSS-78) with respect to monthly climatological 1955–2012 salinity fields from WOA13v2 [yearly average (gray contours at 0.5 intervals), PSS-78]. (b) Difference of 2016 and 2015 surface salinity maps (colors, PSS-78 yr⁻¹). White ocean areas are too data-poor (retaining <80% of a large-scale signal) to map. (c) Map of local linear trends estimated from annual surface salinity anomalies for 2005–16 (colors, PSS-78 yr⁻¹). Areas with statistically insignificant trends are stippled. All maps are made using Argo data.
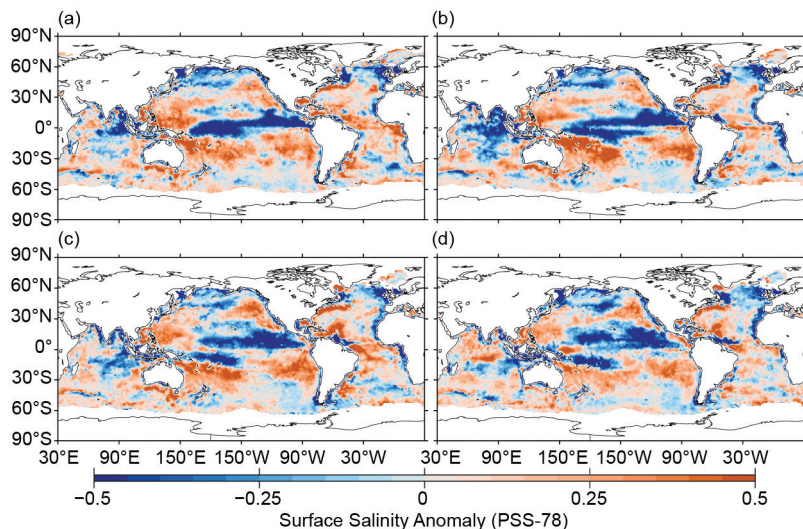
FIG. 3.8. Seasonal maps of SSS anomalies (colors) from monthly blended maps of satellite and in situ salinity data (BASS; Xie et al. 2014) relative to monthly climatological 1955–2012 salinity fields from WOA13v2 for (a) Dec–Feb 2015/16, (b) Mar–May 2016, (c) Jun–Aug 2016, and (d) Sep–Nov 2016. Areas with maximum monthly errors exceeding 10 PSS-78 are left white.

region, fresh anomalies moved poleward over the course of the year, likely reflecting both advection of anomalously fresh waters that built up around the equator owing to strong precipitation and the eastward migration of the western Pacific fresh pool during the 2015/16 El Niño, and subsequent upwelling of saltier water along the equator and reductions of precipitation in the eastern equatorial Pacific with the transition to weak La Niña conditions by the end of 2016.

Sea surface salinity trends for 2005–16 exhibit large-scale patterns in all three oceans (Fig. 3.7c). These trends are estimated by local linear fits to annual average SSS maps from Argo data with a starting year of 2005, because that is when Argo coverage became near-global. There are regions of increasing salinity near the subtropical salinity maxima in each basin, except in the eastern subtropical North Atlantic. In the Pacific, this increasing salinity trend is at lower latitudes in the west than in the east. In contrast, there are regions in the Southern Ocean and the subpolar North Atlantic and North Pacific where the trend is toward freshening. Again, these patterns are reminiscent of the multidecadal changes discussed above and suggest a discernible intensification of the hydrological cycle over the ocean over the last dozen years. However, the freshening trend in much of the subpolar North Atlantic is roughly coincident with a trend toward low upper ocean heat content (see Fig. 3.4c), suggesting an eastward expansion of the subpolar gyre that may be linked to reductions in the AMOC over the past decade (Section 3h). In

addition, the freshening trend in the eastern Indian Ocean is likely owing to a lingering signature of the strong 2010–12 La Niña, refreshed by anomalously strong precipitation in 2016 (see Fig. 3.12). Freshening trends in the eastern tropical Pacific are likely owing to interannual ENSO variability and not necessarily reflective of a long-term trend. The region to the northwest of the Gulf Stream and in the Gulf of Mexico is trending strongly saltier, as well as warmer (Section 3c).

3) SUBSURFACE SALINITY—J. Reagan, T. Boyer, C. Schmid, and R. Locarnini

The 2016 Atlantic Ocean basin-average monthly salinity anomaly pattern (Fig. 3.9a) is similar to the previous decade, with large (>0.05) salty anomalies in the upper 200 m decreasing with depth to little/no change near 700 m and very weak (±0.005) anomalies between 700 and
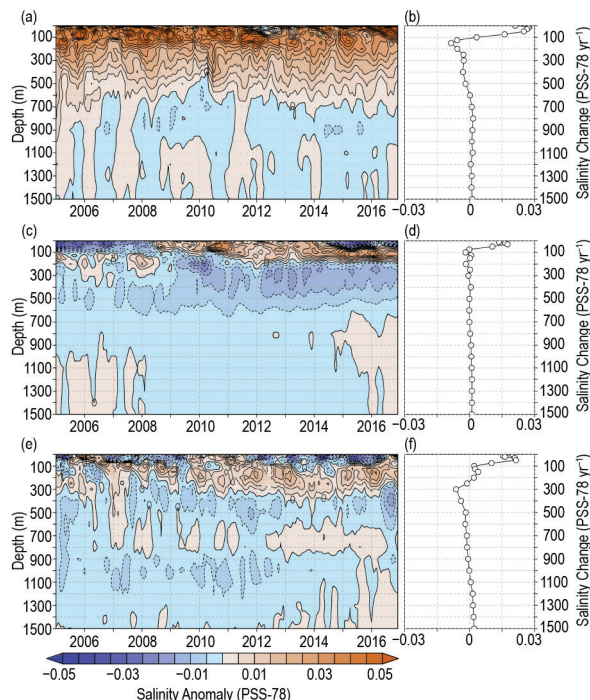

FIG. 3.9. Average monthly ocean salinity anomalies from 0–1500 m for the (a) Atlantic from 2005–16 and (b) the change from 2015 to 2016; (c) Pacific from 2005–16 and (d) the change from 2015 to 2016; and (e) Indian from 2005–2016 and (f) the change from 2015 to 2016. Data were smoothed using a 3-month running mean. Anomalies are relative to the long-term WOA13v2 monthly salinity climatology (Zweng et al. 2013).

1500 m. From 2015 to 2016, salinity increased in the upper 100 m with a maximum increase of ~0.03 near the surface (Fig. 3.9b). From 125 to 600 m, 2016 was slightly fresher than 2015 with a maximum decrease of ~ −0.01 at 150 m.

The upper 30 m of the Pacific Ocean has been fresh since mid-2014, with the exception of weak (±0.005) anomalies in early 2016 (Fig. 3.9c). This pattern contrasts with positive near-surface salinity anomalies from mid-2008 through mid-2014 (Fig. 3.9c). Salty anomalies from 100 to 200 m have been persistent since mid-2011, as have fresh anomalies (< −0.005) from 200 to 500 m since 2009. From 2015 to 2016, salinity increased in the upper 75 m, approaching ~0.02 at 30 m (Fig. 3.9d), in stark contrast to the freshening that was seen between 2014 and 2015 (Reagan et al.

Full-depth ocean temperature–salinity profiling is essential for closing global and regional budgets of heat, freshwater, and steric sea level; for quantifying the processes causing sea level change; for accurately estimating the meridional overturning circulations; and for assimilating global ocean reanalyses and initializing ocean forecast systems. Deep-ocean temperature and salinity observations have been limited to sparse shipboard hydrographic sections repeated approximately every decade and even sparser deep ocean moorings. The need for more frequent sampling of the full ocean volume has long been recognized by the scientific community but has not, until recently, become practical.

Measuring the variability of temperature and salinity in the deep ocean is technically challenging. Deep-ocean properties show significant large-scale trends on decadal time scales in some deep basins, with the strongest anomalies at high latitudes near water mass formation regions (Purkey and Johnson 2010, 2013; Desbruyères et al. 2016). The Argo Program's international partnership proposes to meet the technical challenge by deploying a new generation of Deep Argo floats globally. At present, Argo operates a total of nearly 4000 floats, homogeneously distributed over the global ocean, measuring temperature and salinity profiles to 2000-m depth. Deep Argo will extend conventional Argo sampling to the ocean bottom.

A Deep Argo workshop held in May 2015 articulated key scientific issues, initiated implementation planning for a global Deep Argo array, and identified broad-scale requirements for Deep Argo float measurement of temperature, salinity, and ocean circulation (Zilberman and Maze 2015). Deep Argo will consist of about 1200 floats distributed globally at 5° latitude × 5° longitude spacing. Deep Argo floats will sample the water column from the sea surface to 4000 or 6000 m, depending on the float model used, every 15 days. Statistical analysis indicates that such an array will significantly reduce uncertainties in the global decadal trends in ocean heat content and the steric contribution to sea level rise (Johnson et al. 2015b). The standard error of the trend in global ocean heat content for the 2000–6000 m depth range will decrease to ±3 TW (1 TW = 10^{12} W) using Deep Argo data, down from ±17 TW
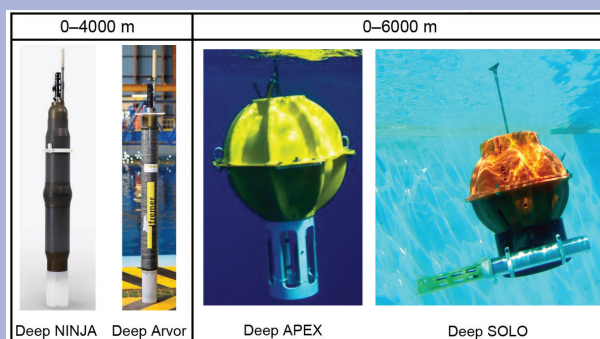

Fɪɢ. SB3.2. Deep Argo float models: Deep NINJA, Deep Arvor, Deep APEX, and Deep SOLO.

based on repeat hydrographic transects. With 15-day cycling, the deep Argo array will have a refresh time, based on float battery energy capacity and consumption, of five years, similar to the 0–2000 m Argo array.

The implementation of a sustainable Deep Argo array will not rely on a single float design. Technology advances have provided pressure housings, pumping systems, and other float components capable of operation at abyssal pressures. Four Deep Argo float models have been developed (Fig. SB3.2), including the 6000-m Deep SOLO (U.S.) and Deep APEX (U.S.) floats, and the 4000-m Deep Arvor (France) and Deep NINJA (Japan) floats. Comparisons of these Deep Argo float models are ongoing to assess their performance, robustness, and cost-effectiveness. Conductivity–temperature–depth (CTD) sensors mounted on Deep Argo floats include an extended-depth version of the SeaBird Electronics SBE-41 on Deep Arvor and Deep NINJA, and the new SBE-61 on Deep SOLO and Deep APEX. Initial results from SBE-61 CTDs in the southwest Pacific indicate that the sensors are stable in abyssal temperature/salinity characteristics, to ±0.001 PSS-78 for more than a year, at constant potential temperature (Fig. SB3.3). These instruments have not yet achieved the absolute accuracy targets set for them (0.001°C, 0.002 PSS-78, and 3 dbar) but are approaching those standards. Additional validation experiments are planned for SBE-41 and SBE-61 CTDs.
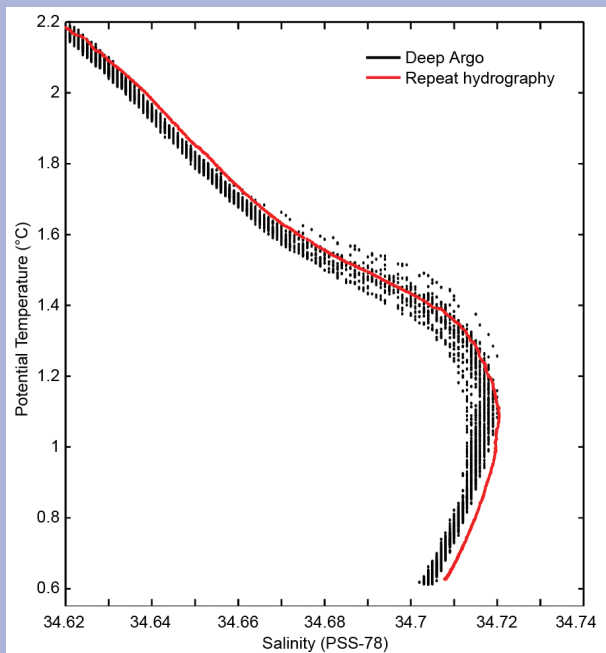
FIG. SB3.3. Temperature/salinity (Θ/S) relationship in the southwest Pacific basin. Black symbols indicate 75 Deep SOLO float profiles spread over 30.4°–35.2°S and 172.8°–174.5°W between Feb 2016 and Jan 2017 (www.usgodae.org/ftp/outgoing/argo/dac /aoml/5902447). The red line is a single cast at 35°S from the P15S repeat hydrographic transect of June 2016 (Source: data courtesy of Bernadette Sloyan, CSIRO.)

Several national programs are now deploying regional pilot Deep Argo arrays to demonstrate the feasibility, capabilities, and scientific value of full-depth global ocean observations, and to validate the accuracy of the CTD data against the requirements for abyssal sampling. Results from the pilot arrays are being assessed to revisit the global design of Deep Argo and its objectives. As of February 2017 there were 64 Deep Argo floats either active or registered for deployment in the next few months, including 33 Deep SOLOs, 3 Deep APEXs,

5 Deep NINJAs, and 23 Deep Arvors (Fig. SB3.4). Present Deep Argo pilot arrays are in the North Atlantic, southwest Pacific, Indian, and Southern Oceans. These arrays will be supplemented with additional floats for increasing their areal extent, and an additional pilot array is planned for the Brazil basin in the South Atlantic. The array in the south Australian basin will be extended poleward into the Australian Antarctic basin. Overall, the locations of pilot arrays have been chosen to include regions having stable abyssal temperature–salinity relations and ample hydrographic reference data for CTD validation, regions with previously identified abyssal warming trends, and regions close to water mass formation zones. In the next few years, the expansion of regional pilot arrays will grow toward global implementation of the Deep Argo Program.
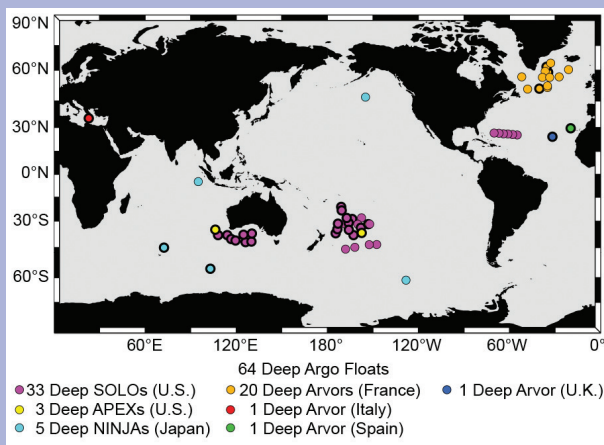

FIG. SB3.4. Location of active Deep Argo floats in Feb 2017 (rounded symbols with thick black contours): 19 Deep SOLOs (U.S.), 3 Deep APEXs (U.S.), 2 Deep NINJAs (Japan), 3 Deep Arvors (France), 1 Deep Arvor (Italy), 1 Deep Arvor (Spain), and 1 Deep Arvor (U.K.). Location of deployments scheduled later in 2017 (rounded symbols with thin black contours) for registered Deep Argo floats: 14 Deep SOLOs (U.S.), 3 Deep NINJAs (Japan), and 17 Deep Arvors (France). (Source: www.jcommops.org.)

2016). This change is likely related to the transition from a strong El Niño in 2015 to a weak La Niña in 2016 and the associated equatorial precipitation (see Fig. 3.12) and wind stress changes (see Fig. 3.13).

Through mid-2016 the Indian Ocean continued to show a similar salinity anomaly structure to that of the previous four years in the upper 300 m, with a fresh surface anomaly from 0 to 75 m and a salty

subsurface anomaly from 100 to 300 m (Fig. 3.9e). However, from mid-2016 onward, this salty subsurface anomaly extended from the surface down to ~250 m depth. From 2015 to 2016 salinity increased from 0 to 200 m, with a maximum of about 0.02 at 50 m, while freshening occurred from 250 to 500 m, with a maximum of ~ −0.008 at 300 m (Fig. 3.9f).

Zonally averaged salinity in the upper 75 m of the tropical Atlantic (2°S–22°N) increased by at least 0.06 from 2015 to 2016 (Fig. 3.10a), with a maximum (~0.12) at the surface between 10° and 16°N. This band is primarily responsible for the near-surface positive salinity anomaly during 2016 (Fig. 3.9b). There is notable freshening (< −0.03) from 0 to 50 m centered at 41°N, but it is shifted south and confined to a smaller region than prior years (e.g., 2015 minus 2014, see Reagan et al. 2016). Additionally, there is strong (< −0.06) subsurface freshening from 100 to 225 m in the South Atlantic from 22° to 15°S and weaker freshening (~ −0.03) in the North Atlantic from 21° to 32°N and 55° to 62°N along similar depths, which are the main contributors to the 100–300 m subsurface freshening (Fig. 3.9b).

Zonally averaged salinity changes in the Pacific from 2015 to 2016 (Fig. 3.10b) show strong (< −0.06) freshening north of 60°N from 0 to 110 m and 160 to 250 m in the northern portions of the Bering Sea. Additionally, there is freshening from 0 to 200 m between 39° and 47°N, exceeding −0.12 at 125 m. The tropical Pacific experienced salinification (> 0.03) in the upper 50 m between 3°S and 17°N from 2015 to 2016 and freshening (< −0.03) in both poleward directions from 18° to 27°N (extending and deepening to the south reaching ~250 m at around 8°S) and 12° to 4°S, which is a direct reflection of the transition from a strong 2015/16 El Niño to a weak 2016 La Niña (as discussed in Section 3d2). Farther south, there is a broad region (between 30° and 13°S) of salinification in the upper 100 m, deepening to 150 m around 10°S.

Zonally averaged salinity changes in the Indian Ocean from 2015 to 2016 (Fig. 3.10c) show freshening (< −0.03) between 10° and 15°N in the upper 100 m, with maximum freshening (< −0.09) occurring at the near-surface (0–30 m). This freshening was primarily located in the Bay of Bengal (see Fig. 3.7b) and may be associated with increased river runoff due to a stronger India monsoon in 2016 than in 2015 (see Fig. 7.47). Salinification occurred in the upper 100 m from 16° to 25°N, with a maximum exceeding 0.18 at 50 m and a narrow swath extending to 250 m at 18°N. Between 0° and 8°N and between 18° and 2°S the salinity increased (> 0.03), with the former extending down to ~75 m and the latter to ~100 m. Finally, freshening (< −0.03) occurred between 45° and 40°S in the upper ~125 m. The broad-scale salinification in the upper 200 m of the southern Indian Ocean in conjunction with the large salinification around 18°N were the primary contributors to the near-surface salinification (Fig. 3.9f).
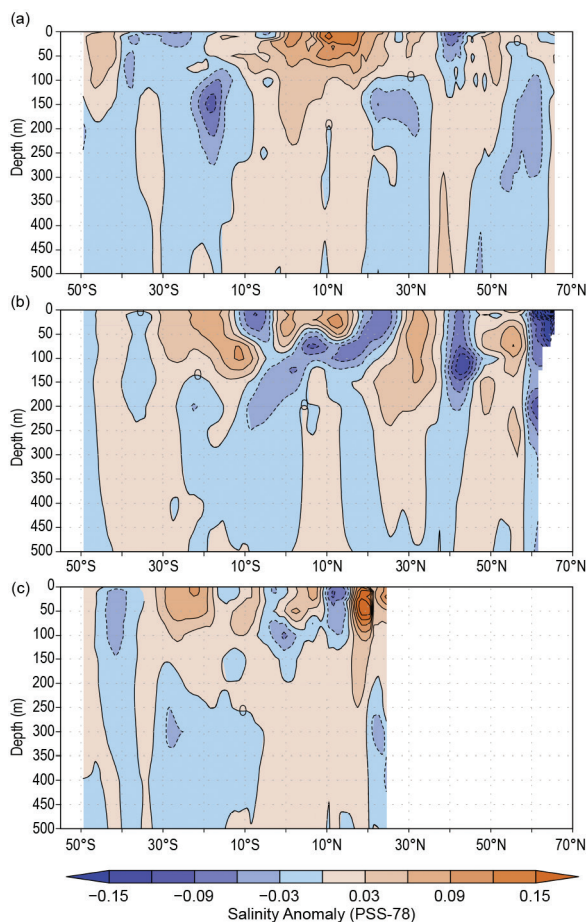

FIG. 3.10. Difference between the 2016 and 2015 zonally averaged monthly salinity anomalies from 0 to 500 m color contoured at 0.03 intervals (black lines, zero contour bold) for the (a) Atlantic, (b) Pacific, and (c) Indian Oceans. Anomalies are relative to the long-term WOA13v2 monthly salinity climatology (Zweng et al. 2013).

e. *Global ocean heat, freshwater, and momentum fluxes*—L. Yu, X. Jin, S. Kato, N. G. Loeb, P. W. Stackhouse, R. A. Weller, and A. C. Wilber

The ocean and the atmosphere communicate physically via interfacial exchanges of heat, freshwater, and momentum. These air–sea fluxes are the primary mechanisms for keeping the global climate system in balance with the incoming insolation at Earth's surface. Most of the shortwave radiation (SW) absorbed by the ocean's surface is vented into the atmosphere by three processes: longwave radiation (LW), turbulent heat loss by evaporation (latent heat flux, or LH) and by conduction (sensible heat flux, or SH). The residual heat is stored in the ocean and transported by the ocean's surface circulation, forced primarily by the momentum transferred to the ocean by wind stress, as well as diffusive processes. Evaporation connects heat and moisture transfers,

and the latter, together with precipitation, determines the local surface freshwater flux. Identifying changes in the air–sea fluxes is essential to deciphering observed changes in ocean circulation and its transport of heat and salt from the tropics to the poles.

Air–sea heat flux, freshwater flux, and wind stress in 2016 and their relationships with ocean surface variables are assessed. The net surface heat flux, Q_{net}, is the sum of four terms: SW + LW + LH + SH. The net surface freshwater flux into the ocean (neglecting riverine and glacial fluxes from land) is simply precipitation (P) minus evaporation (E), or the $P - E$ flux. Wind stress is computed from satellite wind retrievals using the bulk parameterization of Edson et al. (2013). The production of the global maps of Q_{net} (Fig. 3.11), $P - E$ (Fig. 3.12), and wind stress (Fig. 3.13) in 2016 and the long-term record of surface flux variations (see Fig. 3.14) are made possible through integrating multigroup efforts. Ocean-surface LH, SH, E, and wind stress are from the Objectively Analyzed Air–Sea fluxes (OAFlux; http://oaflux .whoi.edu/) project's satellite-derived, high-resolution (hereafter OAFlux-HR) products (Yu and Jin 2012, 2014; Jin and Yu 2013). Surface SW and LW radiative fluxes are from the Clouds and the Earth's Radiant Energy Systems (CERES) Fast Longwave And Shortwave Radiative Fluxes (FLASHFlux; https://ceres.larc .nasa.gov/products.php?product=FLASHFlux) Ed3A product (Stackhouse et al. 2006). Global P is from the Global Precipitation Climatology Project (GCPC; http://gpcp.umd.edu) version 2.3 products (Adler

et al. 2003). The CERES Energy Balanced and Filled (EBAF) surface SW and LW version 2.8 products (http://ceres.larc.nasa.gov; Kato et al. 2013) are used in the time series analysis.

1) Surface heat fluxes

The dominant feature in the 2016 Q_{net} anomalies (Fig. 3.11a) was the broad-scale positive Q_{net} region in the equatorial and South Pacific, where the ocean received more than 10 W m^{-2} of anomalous heating from the atmosphere. The anomaly pattern may be associated with the transition from the strong 2015/16 El Niño to a weak La Niña in late 2016 (see Fig. 3.2). Two distinct zonal bands of positive values were present in the equatorial Pacific, both in the 2016 Q_{net} anomalies (Fig. 3.11a) and in the 2016 minus 2015 Q_{net} tendencies (Fig. 3.11b). One band was located about 3–5 degrees of latitude north of the equator, and the other centered on the central and eastern equatorial sector. The Q_{net} anomaly band off the equator is attributable to the change in surface radiation. The 2016 minus 2015 (SW+LW) tendencies (Fig. 3.11c) in the equatorial region were structured along the ITCZ mean position, with positive values stretching across the entire Pacific and negative values over the far western Pacific and the eastern Indian Ocean. This SW+LW tendency pattern is consistent with the 2016 minus 2015 P tendency pattern (Fig. 3.12d), so SW+LW increased in area of reduced ITCZ rainfall and, conversely, SW+LW reduced in area of increased ITCZ rainfall. The close association between the SW+LW and P tendencies along the ITCZ reflects the reorganization of the tropical convection in response to the transition from El Niño to La Niña (Rasmusson and Wallace 1983). On the other hand, the 2016 Q_{net} anomaly band centered on the equator is associated primarily with LH+SH tendencies (Fig. 3.11d). The surface cooling during the development of the 2016 La Niña was at maximum in the central equatorial sector, with SST tendency anomalies at about 1.5°C (see Fig. 3.1b). The cooler sea surface produced
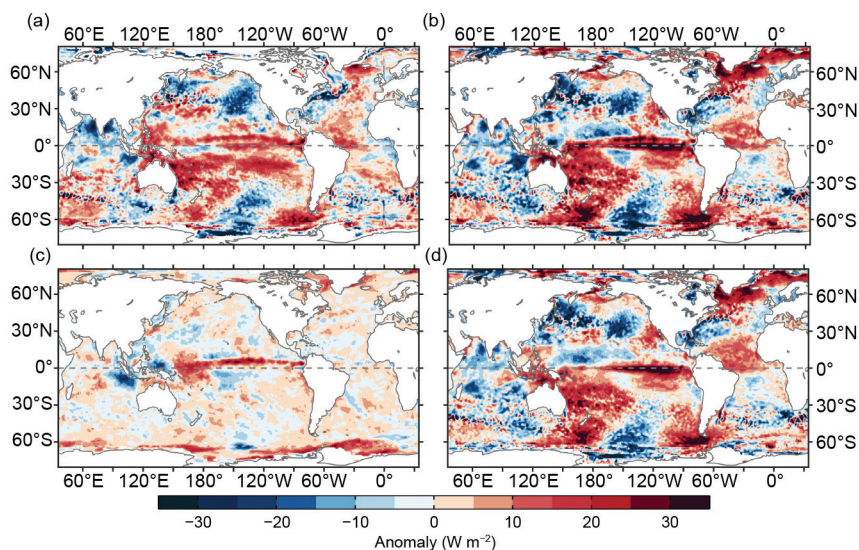

Fig. 3.11. (a) Surface heat flux (Q_{net}) anomalies (W m^{-2}) for 2016 relative to a 5-yr (2010–14) mean. Positive values denote ocean heat gain. (b) 2016 minus 2015 tendencies for Q_{net}, (c) surface radiation (SW+LW), and (d) turbulent heat fluxes (LH+SH), respectively. Positive tendencies denote more ocean heat gain in 2016 than in 2015. LH+SH are produced by the OAFlux high-resolution (HR) satellite-based analysis and SW+LW by the NASA FLASHFlux project.

less evaporation, leading to a reduction of turbulent latent and sensible heat loss and hence a warming effect on the ocean. The relation of LH+SH tendencies to SST tendencies indicates that the surface fluxes provided a negative feedback, suppressing the development of a La Niña cooling in the central and eastern equatorial Pacific.

In the South Pacific outside of the equatorial band, the 2016 minus 2015 (LH+SH) tendencies had a warming effect over the eastern and western portions of the basin, but a cooling effect over the central basin. The SW+LW tendency pattern was similar, albeit with a much smaller (~5 W m⁻²) magnitude. Both LH+SH and SW+LW tendencies correlate positively with those of SST, which is in stark contrast to their negative correlation in the equatorial region. The positive correlation suggests that the regional SST tendencies were a result of the WES (wind–evaporation–SST) positive feedback associated with anomalous southeast trade winds (Fig. 3.13b). Winds facilitate the rate of evaporation, increasing latent heat loss in stronger winds and reducing it in weaker winds. SST warmed in places where wind speeds weakened and latent heat loss was reduced, and cooled in places where wind speeds strengthened and latent heat loss was increased (Figs. 3.1b, 3.12d, 3.13b). Surface heat fluxes have dual effects on SST: they could be a response to SST anomalies, such as in the equatorial Pacific, and they could also be a forcing of SST anomalies, such as in the South Pacific.

For all three basins in the Northern Hemisphere, surface heat fluxes acted predominantly as a forcing of regional SST anomalies through the WES mechanism. For instance, the band of strong surface cooling (i.e., SST cooling tendency) in the midlatitude North Pacific between 30° and 50°N corresponds to the band of enhanced LH+SH loss as a result of strengthened westerly winds. Similar correlations are also displayed in the North Atlantic, where a tripole-like pattern (with extrema broadly in the tropics, subtropics, and subpolar regions) in the Q_{net} anomaly field is associated with a tripole pattern of wind speed anomalies
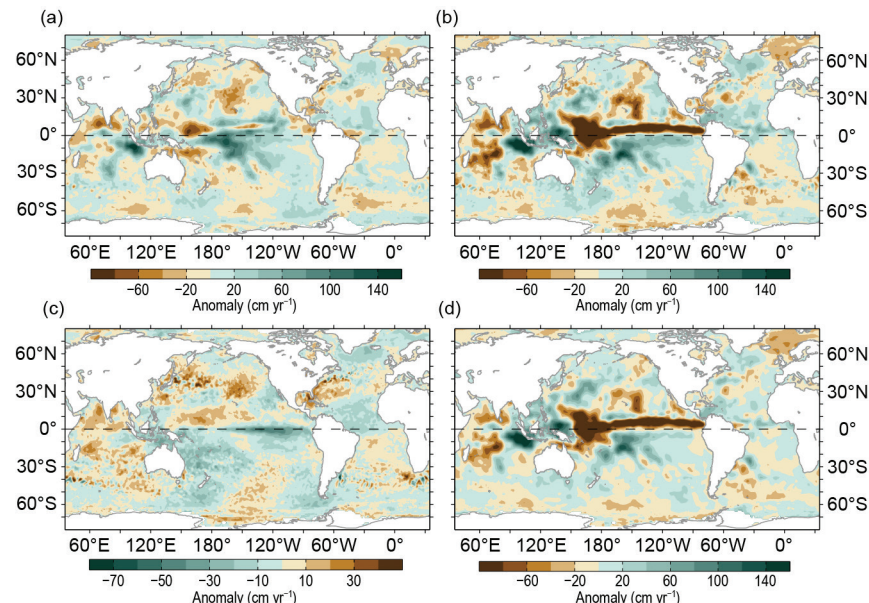

Fig. 3.12. (a) Surface freshwater (P−E) flux anomalies (cm yr⁻¹) for 2016 relative to the 1988–2014 climatology. 2016 minus 2015 tendencies for (b) P−E, (c) evaporation (E), and (d) precipitation (P). Green colors denote anomalous ocean moisture gain, and browns denote loss, consistent with the reversal of the color scheme in (c). P is computed from the GPCP version 2.3 product, and E from OAFlux-HR satellite-based analysis.

of opposite sign, and less clearly with SSTA. In the tropical Indian Ocean, the surface cooling north of 15°S is clearly a result of the WES mechanism, as the strengthened monsoonal winds induced stronger LH+SH loss that effectively cooled the ocean surface.

2) Surface freshwater fluxes

The 2016 P−E anomaly patterns are characterized by significant P anomalies in the tropical Pacific and Indian Oceans (Fig. 3.12). In response to the transition from El Niño to La Niña, the ITCZ rainfall band that was equatorward-strengthened during the 2015/16 El Niño weakened considerably in 2016, leading to a significant reduction in P. This is evident in the 2016 minus 2015 P tendency pattern, where a zonal band of strong dry tendencies stretched across the entire equatorial Pacific along the ITCZ (Fig. 3.12d). The magnitude of the dry tendencies exceeded one meter over one year and dominated the P−E tendencies in the tropical Pacific (Fig. 3.12b). At the same time, the far western Pacific and the eastern equatorial Indian Ocean received more rainfall (Fig. 3.12), associated with the enhanced regional deep convection during the development of the weak 2016 La Niña. The band of strong dry P−E tendency along the ITCZ, although a striking feature, is not a major climate anomaly in the context of the 27-year (1988–2014) climatological reference. In 2016, the tropical Pacific gained about

0.5 m of freshwater compared to the climatological mean condition.

The western tropical Indian Ocean had a freshwater deficit (Fig 3.12) of about 0.3 m in 2016, attributed to both enhanced evaporation and weakened precipitation. The pattern of change seems to be ENSO-induced. The enhanced deep convection over the Indo-Pacific region drew the confluence of surface winds, which led to an acceleration of the surface branch of the Walker circulation. The strengthening of the surface winds over the tropical Indian Ocean (Figs. 3.13a,b) enhanced the regional evaporation.

A tripole-like pattern in the North Atlantic (with signs changing broadly among the tropical, subtropical, and subpolar regions) is evident in both E and P tendency (Fig. 3.12), showing that E increased in regions where P decreased, and reduced in regions where P increased. Coherent E and P tendency patterns are also apparent in the South Atlantic and the extratropical Pacific.

3) WIND STRESS

The 2016 wind stress anomalies were mostly zonally aligned, reflecting the global distribution of the near-surface wind system (Figs. 3.13a,b). The most significant anomalies were the strengthened westerly winds in the midlatitude North Pacific (30°–50°N), where the strengthened winds enhanced LH+SH heat loss and caused surface cooling through the WES feedback. Significant wind anomalies were also observed along the westerly wind band in the Southern Ocean (30°–60°S), where wind anomalies were structured in a wavelike pattern with alternating positive and negative signs. In the equatorial region, the enhanced deep convection associated with the transition from El Niño to La Niña in the Indo-Pacific region led to an enhanced Walker circulation, and consequently, stronger easterly anomalies in the equatorial Pacific and stronger westerly anomalies in the equatorial Indian Ocean (Rasmusson and Carpenter 1982). In the South Pacific, the southeast trade winds became weaker. It is yet to be examined whether the weakened trades were associated with the decaying El Niño or caused by the warm PDO phase that persisted through 2016 (see Fig. 3.1a).

Spatial variations of winds around the globe cause divergence and convergence of the Ekman transport, leading to a vertical velocity, denoted by Ekman pumping (downward) or suction (upward) velocity W_{EK}, at the base of the Ekman layer. Computation of W_{EK} follows the equation: $W_{EK} = 1/\rho \nabla \times (\tau/f)$, where ρ is the density and f the Coriolis force. The 2016 minus 2015 W_{EK} tendencies (Fig. 3.13d) resulted in strong downwelling (negative) anomalies in the vicinity of the Pacific ITCZ mean position (3°–5°N) and strong upwelling (positive) anomalies in the eastern equatorial Indian Ocean. This pattern corresponds well with the change of trade winds during the transition from El Niño to La Niña. Outside of the tropical region, the strengthened westerly band in the midlatitude North Pacific induced a band of downwelling anomalies (negative) on its southern flank and a band of upwelling anomalies (positive) on its northern flank. In the North Atlantic, W_{EK} anomalies (Fig. 3.13c) were characterized by a tripole pattern, with positive upwelling anomalies from 40°–60°N and negative downwelling anomalies both poleward of 60°N and from 15°–30°N.

FIG. 3.13. (a) Wind stress magnitude (colors) and vector anomalies (N m⁻²) for 2016 relative to 1988–2014 climatology, (b) 2016 minus 2015 tendencies in wind stress, (c) Ekman vertical velocity (W_EK) anomalies for 2016 relative to 1988–2014 climatology, and (d) 2016 minus 2015 tendencies in W_EK. In (c) and (d), positive values denote upwelling tendency, and negative downwelling; units are cm day⁻¹. Winds are computed from the OAFlux-HR satellite-based vector wind analysis.

4) LONG-TERM PERSPECTIVE

Annual-mean time series of Q_{net}, $P – E$, and wind stress averaged over the global ice-free oceans (Fig. 3.14) provide a decadal perspective on the ocean surface forcing functions in 2016. The Q_{net} time series were
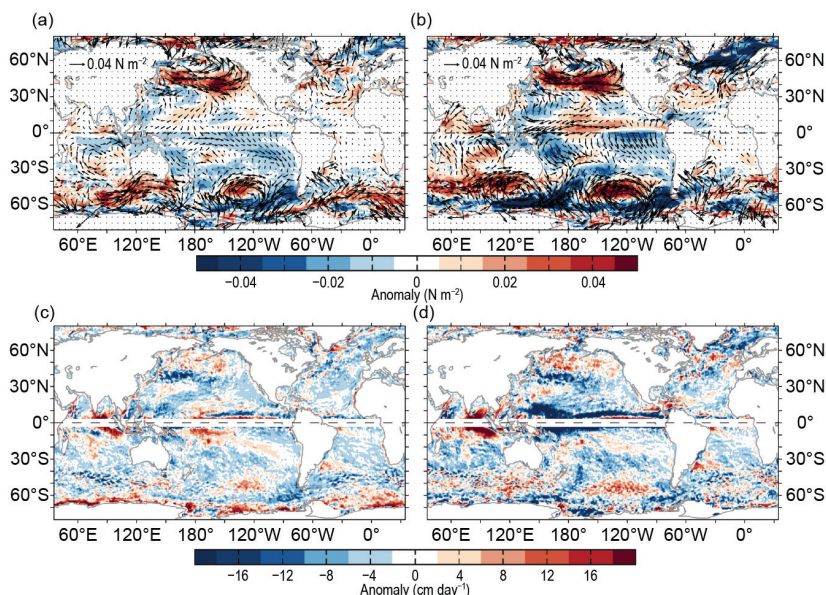
constructed for the period from 2001 onward, using the available period of the CERES EBAF dataset. The time series of $P - E$ and wind stress started from the availability of SSM/I observations in 1988. The Q_{net} time series trended slightly higher in recent years after a major dip in 2008. These Q_{net} fluctuations may be related to ENSO, with the ocean gaining more heat as El Niño strengthens and less as La Niña builds (Johnson and Birnbaum 2017). A similar dip is also present in $P - E$ time series and wind time series, except that the dip in wind occurred one year later in 2009. The $P - E$ time series variations again may be owing to changes in transfers of water between land and sea with ENSO (e.g., Cazenave et al. 2012).

The $P - E$ time series is up slightly in 2016, presumably reflecting El Niño's influence on tropical oceanic precipitation. To first order, the GPCP precipitation dataset shows that changes over land and ocean during El Niño or La Niña years approximately balance, giving a global time series that is more nearly constant than the land-only or ocean-only time series. Over the 29-year period, the $P - E$ time series shows a slight decrease during the 1990s but no obvious trend thereafter. A strengthening of the global winds in the 1990s is also indicated in the global wind stress time series of 29 years. The global average wind stress remains near steady in recent years.

f. Sea level variability and change—P. R. Thompson, M. A. Merrifield , E. Leuliette, W. Sweet, D. P. Chambers, B. D. Hamlington, S. Jevrejeva, J. J. Marra, G. T. Mitchum, and R. S. Nerem

Global mean sea level (GMSL) during 2016 became the highest annual average in the satellite altimetry record (1993–present), rising to 82 mm above the 1993 average (Fig. 3.15a). This marks the sixth consecutive year (and 21st out of the last 23) that GMSL increased relative to the previous year. The new high reflects the ongoing multidecadal trend in GMSL during the satellite altimetry era, 3.4 (±0.4) mm yr^{-1} (Fig. 3.15a), as well as the continuation of the 2015/16 El Niño into spring 2016 (see Fig. 3.2).

Variations in GMSL (Fig. 3.15a) result from changes in both the mass and density of the global ocean (Leuliette and Willis 2011; Chambers et al. 2017). From 2005 to present, increasing global ocean mass observed by the NASA Gravity Recovery and Climate Experiment (GRACE) contributed approximately two-thirds of the GMSL trend, 2.1 (±0.4) mm yr^{-1}. The positive trend in ocean mass primarily resulted from melting of glaciers and ice sheets (see Chapters 5e,f), but these contributions from land ice were partially offset by increased hydrological storage
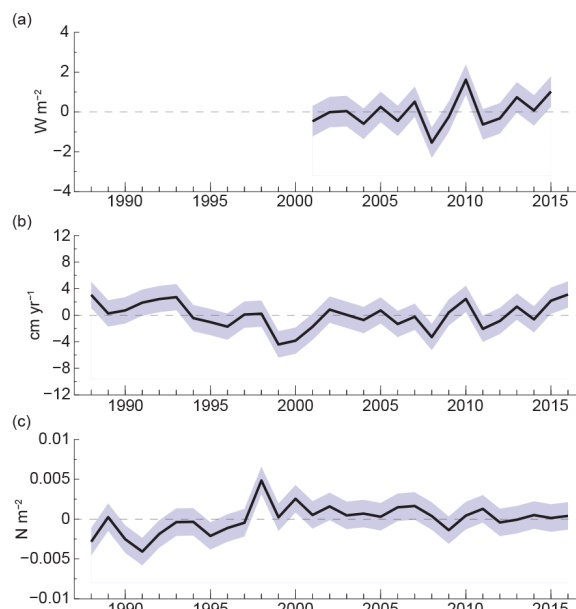

Fig. 3.14. **Annual-mean time series of global averages of (a) net surface heat flux (Q$_{net}$; W m^{-2}) from the combination of CERES EBAF SW+LW and OAFlux-HR LH+SH, (b) net freshwater flux ($P-E$; cm yr^{-1}) from the combination of GPCP P and OAFlux-HR E, and (c) wind stress magnitude (N m^{-2}) from OAFlux-HR vector wind analysis. Shaded area denotes one std. dev. of annual-mean variability.**

of fresh water on land, −0.7 (±0.2) mm yr^{-1} (Reager et al. 2016). Mostly owing to ocean warming, steric (i.e., density-related) sea level rise, 1.0 (±0.2) mm yr^{-1}, has been observed by the Argo profiling float array and accounts for the balance of the GMSL trend since 2005.

Regional sea level trends differ substantially from the global mean trend (Fig. 3.15b). Since the 1993 advent of satellite altimetry, the Indian Ocean and western Pacific have experienced enhanced sea level rise relative to the global average (3 to 7 mm yr^{-1}) while the eastern Pacific and polar regions experienced less sea level rise or even sea level fall (−1 to 3 mm yr^{-1}). The east–west trend difference across the Pacific results from strengthening trade winds and a multidecadal trend toward the negative phase of the PDO during much of the altimetry era (Merrifield 2011; Hamlington et al. 2014). Enhanced trade winds force zonal redistribution of ocean volume across the basin leading to enhanced sea level rise in the west at the expense of regions to the east (Thompson et al. 2014). More recently, beginning with the strong 2010/11 La Niña event and culminating with the recent El Niño, a dramatic reversal occurred in the rates of Pacific sea level change (Hamlington et al. 2016). During 2012–16, much of the eastern Pacific
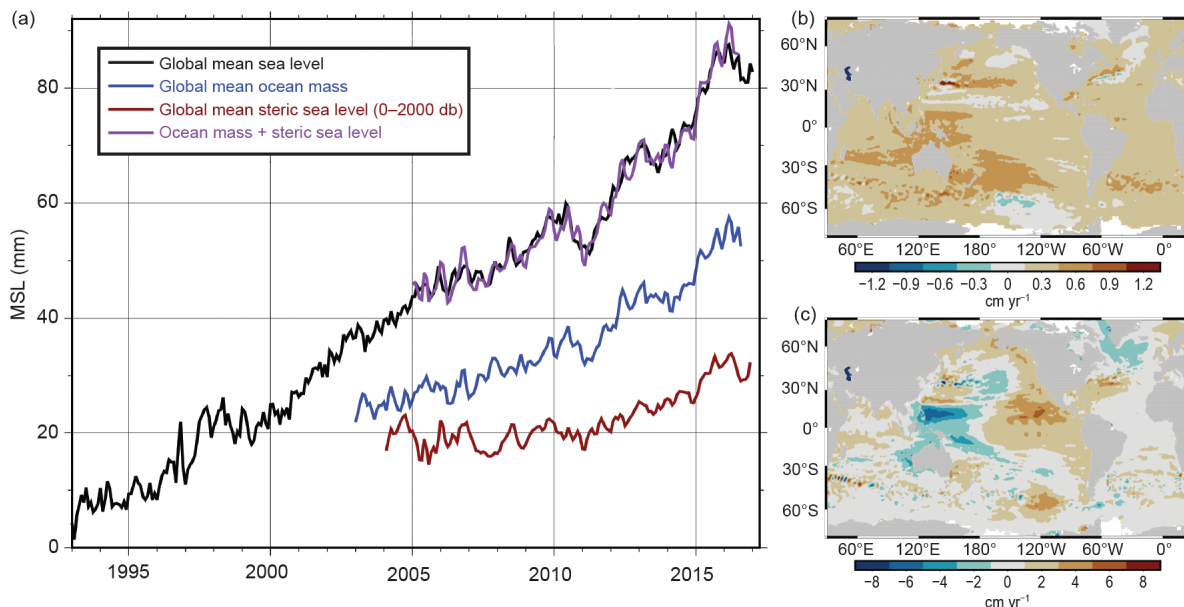
Fig. 3.15. (a) Monthly averaged global mean sea level (mm; black line) observed by satellite altimeters (1993–2016) from the gridded, multi-mission product maintained by the CMEMS (product formerly known as Aviso). Monthly averaged global ocean mass (blue; 2003–Aug 2016) from GRACE. Monthly averaged global mean steric sea level (red; 2004–16) from the Argo profiling float array. Mass plus steric (purple). (b) Linear sea level trends (cm yr^{-1}) from altimetry during 1993–2016. (c) Linear sea level trends (cm yr^{-1}) from altimetry during 2012–16.

experienced 20 to 40 mm yr^{-1} of sea level rise while sea level fell by a similar amount around Southeast Asia and Australia (Fig. 3.15c). Trends in the equatorial and North Indian Ocean did not reverse with the western Pacific, reflecting continued ocean warming since 2004 due to a reduction in wind-forced overturning (Thompson et al. 2016).

In addition to long-term trends, interannual climate variability causes global and regional sea level to deviate from secular trajectories. ENSO is a principal driver of interannual variability in GMSL (Nerem et al. 1999), and the large 2015/16 El Niño caused GMSL to be greater during the past two years than would be expected from the linear trend alone (Fig. 3.15a). During the first half of 2016, a weakened Walker Cell and other ENSO-related teleconnections altered precipitation patterns (particularly at tropical latitudes; see Fig. 2.1i), leading to decreased land-water storage (see Fig. 2.1j) and increased ocean mass (Fig. 3.15a). Similarly, global ocean heat content (OHC) anomalies show a striking warm event in the upper 100 dbar of the global ocean during the course of the El Niño event from late 2015 through early 2016 (see Fig. 3.5). The near-surface OHC anomaly contributes to the positive steric sea level anomaly during the first half of 2016 (Fig. 3.15a). In contrast to OHC, total steric sea level (including thermosteric and halosteric contributions) increased on average during 2016 relative to 2015 due to subsurface fresh-

ening in the northeast Atlantic, South Indian, and Southern Oceans (not shown). The freshening at least partially accounts for the year-over-year increase in GMSL despite the relaxation of El Niño conditions and decrease in OHC throughout 2016.

Regionally, positive annual sea level anomalies spanned most the global ocean during 2016 with prominent exceptions in the western Pacific and subpolar North Atlantic (Fig. 3.16a). The structure of annual anomalies in the Pacific weakly resembles the canonical El Niño pattern, which reflects the transition from typical El Niño structure early in the year (Fig. 3.16c) to mostly neutral conditions by the end of 2016 (Fig. 3.16d). The difference between 2016 and 2015 annual sea level anomalies (Fig. 3.16b; similar to OHC, see Fig. 3.4b) clearly shows the interhemispheric seesaw in the tropical Pacific that tends to occur at the termination of strong El Niño events (Widlansky et al. 2014). Near the end of such events, the weak trade winds typical of El Niño tend to shift southward while an anomalous anticyclone develops in the Philippine Sea. Together, these wind patterns prolong negative sea level anomalies south of the equator that subsequently spread eastward along the equatorial waveguide. In the North Atlantic, negative sea level anomalies during 2016 (Fig. 3.16a) continued a multidecadal cooling trend in the region (Fig. 3.15b; see Fig. 3.4c), perhaps related to weakening of the Atlantic overturning circulation and record low
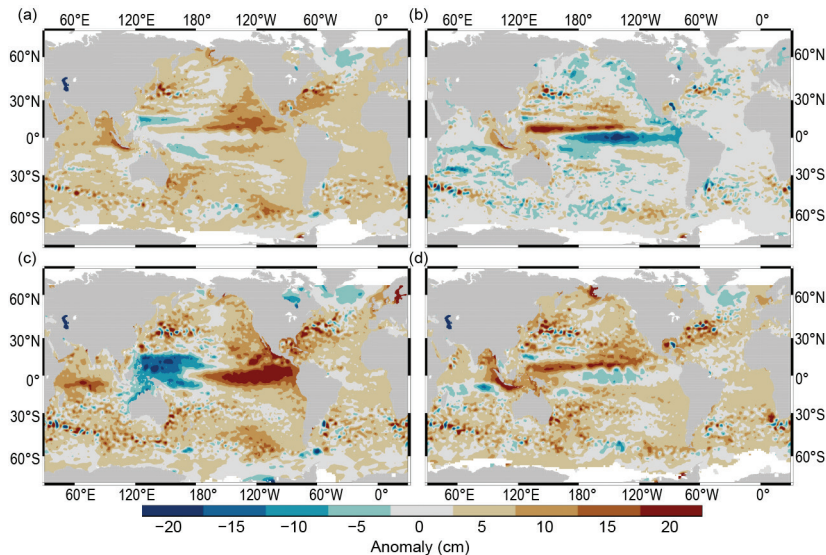
Fig. 3.16. (a) Annual average sea level anomaly during 2016 relative to the average sea level at each location during 1993–2016. (b) Average 2016 sea level anomaly minus 2015. (c) Average sea level anomaly during Dec 2015–Feb 2016 (DJF) relative to the DJF average during 1993–2016. (d) As in (c), but for Sep–Nov 2016. Anomalies are in cm. Altimetry data were obtained from the gridded, multimission product maintained by CMEMS.

calculations in Fig. 3.17 reveals the contribution of synoptic times-cales (i.e., storminess) to sea level extremes in the tide gauge records (not shown). The filtering exercise suggests that increased storminess mostly accounts for the increased number of 2016 extremes along the U.S. northeast and East Asian coastlines and partially accounts for the increase in southern Australia and the tropical Indian Ocean. This leaves background sea level change as the dominant contribution to elevated numbers of sea level extremes in the southeast U.S., Hawaii, and central South Pacific. Along the southeast U.S. coastline, the increase may be related to the hypothesized slow-down of the Florida Current and Gulf Stream during recent decades (Ezer et al. 2013; Sweet et al. 2016), which would tend to raise coastal sea level in the region. Increased numbers of extremes in the central South Pacific most likely relate to multidecadal regional sea level trends (Fig. 3.15b), because the annual anomaly in the region is generally small (Fig. 3.16a) and the number of extremes decreases relative to 2015 (Fig. 3.17c). The opposite is true for Hawaii, where the multidecadal trend is small (Fig. 3.15b), but the annual anomaly is large (Fig. 3.16a) due to Rossby waves emanating from the eastern boundary during mid- to late 2016 in response to ENSO forcing along the equator.

densities in the deep Labrador Sea (Rahmstorf et al. 2015; Robson et al. 2016).

Global and regional mean sea level change affects coastal communities by changing the frequency of positive sea level extremes that cause flooding and erosion. Infrastructure within coastal communities is currently exposed to "nuisance" (associated with minor impacts) tidal flooding at a median height of about 0.5 m above mean higher high water (MHHW) tidal datum (Sweet et al. 2014), which is approximated as the long-term average of daily highest water levels. High-frequency measurements by a global set of tide gauges find that the median of the top 1% of observed daily maximum heights (three to four days per year on average) is also about 0.5 m above MHHW (Fig. 3.17a). During 2016, multiple regions experienced greater-than-average numbers of such sea level extremes: the U.S. East Coast, the central South Pacific, southern Australia, and the tropical Indian Ocean (Fig. 3.17b). The U.S. West Coast did not experience a greater number of sea level extremes despite substantially elevated mean sea levels in the region (Fig. 3.16a). Relative to 2015, spatially coherent increases in sea level extremes occurred over the U.S. northeast coast, Hawaii, portions of East Asia, and southern Australia (Fig. 3.17c).

Two factors can lead to increased numbers of positive sea level extremes: elevated background mean sea level and increased storminess (e.g., Sweet and Park 2014). High-pass filtering the tide gauge observations with a cut-off period of 30 days and then repeating the

g. Surface currents—R. Lumpkin, G. Goni, and K. Dohan

This section describes ocean surface current changes, transports derived from ocean surface currents, and features such as rings inferred from surface currents. Surface currents are obtained from in situ (global array of drogued drifters and moorings) and satellite (altimetry, wind stress, and SST) observations. Transports are derived from a combination of sea height anomaly (from altimetry) and climatological hydrography. See Lumpkin et al. (2012) for details of the datasets used and calculations performed. Anomalies are calculated with respect to the time period 1992–2007. Annually averaged zonal current anomalies and changes in anomalies from the previous year are shown in Fig. 3.18, while seasonal averages are shown in Fig. 3.19. These anomalies are discussed below for individual ocean basins.
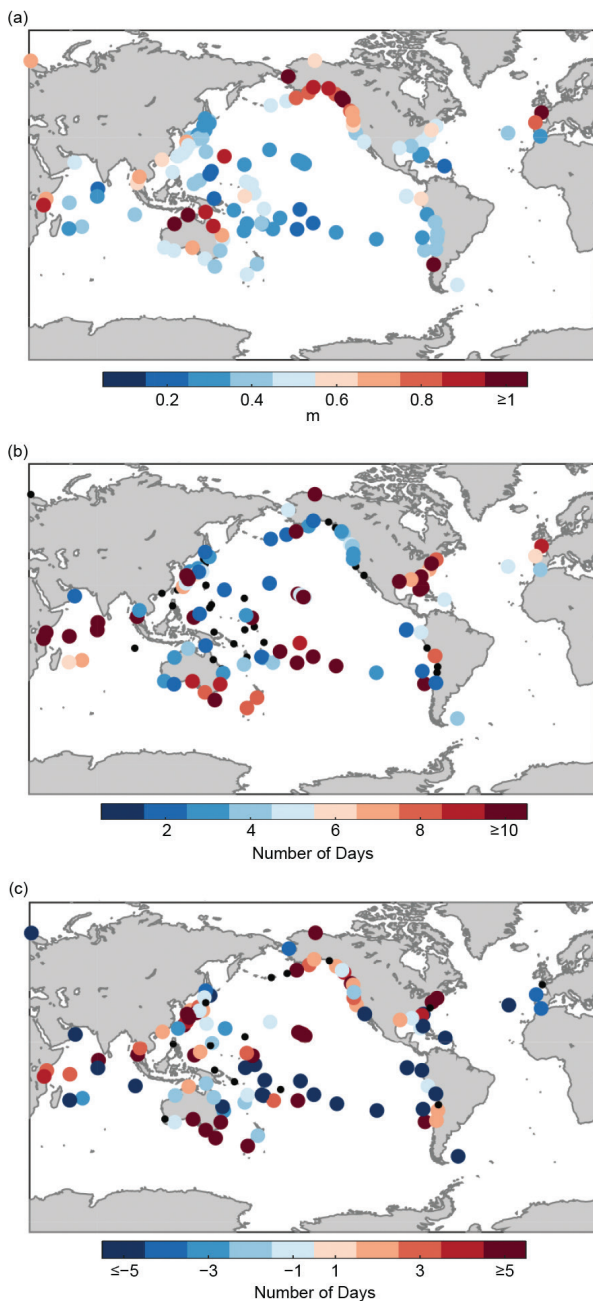
Fig. 3.17. (a) Thresholds defining an extreme sea level anomaly (m) for each station in the presnt analysis. 1% of daily maximum water levels at each station reach heights indicated by the colors in the figure. Units are meters above mean higher high water (MHHW) calculated over 1996–2015. (b) Number of daily maximum water levels during 2016 above the thresholds in (a). Small, black circles in (b) and (c) indicate a value of zero. (c) As in (b), but for 2016 minus 2015. Daily maximum water levels were calculated from hourly tide gauge observations obtained from the University of Hawaii Sea Level Center Fast Delivery database. Only records with at least 80% completeness during 1996–2015 and 80% completeness during 2016 were analyzed.

1) Pacific Ocean

Westward anomalies across the equatorial Pacific, associated with the 2016 La Niña, dominated annual mean current anomalies in the Pacific basin (Fig. 3.18a). These anomalies had an annually averaged value of 12–16 cm s^{-1} between 1°S and 6°N. Farther north, a narrow band of eastward anomalies peaked at 15–17 cm s^{-1} between 9° and 10.5°N, on the northern flank of the climatological North Equatorial Countercurrent (NECC), associated with a northward displacement of that current. Because 2015 was characterized by a reversal of these patterns, that is, intense eastward equatorial anomalies during the 2015/16 El Niño and westward anomalies in a weakened NECC, the 2016 minus 2015 tendencies (Fig. 3.18b) are a magnified version of the 2016 anomalies.

The year 2016 began (Fig. 3.19) with El Niño-related eastward anomalies exceeding 20 cm s^{-1} between 2°S and 5°N in the central basin, with peak anomalies of 40 cm s^{-1} at 3°N. These anomalies had reversed by February, with westward anomalies of 20–30 cm s^{-1} between the equator and 2°N. By March, these anomalies were quite dramatic in the eastern half of the basin, with peak values of 50 cm s^{-1} westward between 100°W and 155°W. As a consequence, the westward flow there increased from 75 cm s^{-1} (the climatological March value) to ~130 cm s^{-1}. Strong westward anomalies persisted and spread westward
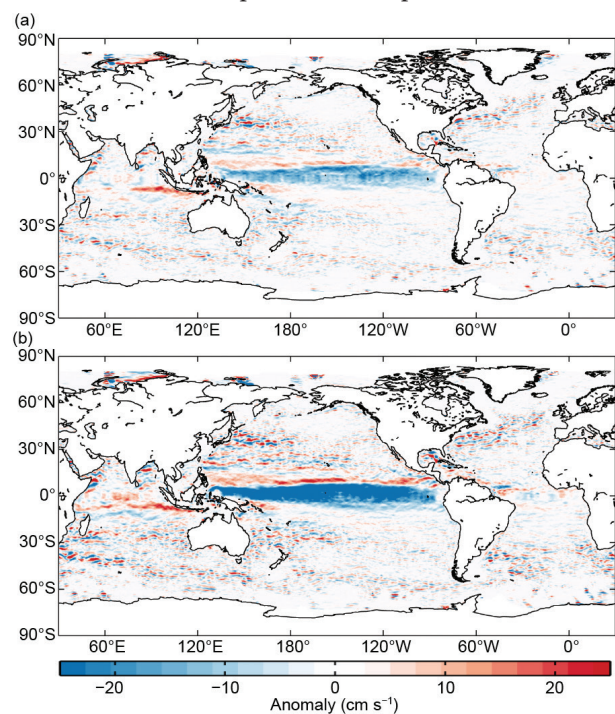

Fig. 3.18. Annually averaged geostrophic zonal current anomalies (cm s^{-1}) for (a) 2016 and (b) 2016 minus 2015 derived from a synthesis of drifters, altimetry, and winds.
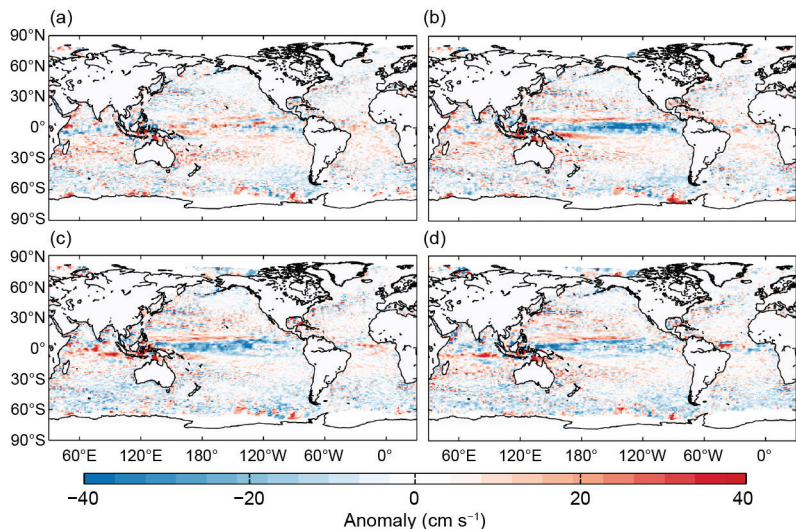
FIG. 3.19. Seasonally averaged zonal geostrophic anomalies (cm s⁻¹) with respect to seasonal climatology, for (a) Dec 2015–Feb 2016, (b) Mar–May 2016, (c) Jun–Aug 2016, and (d) Sep–Nov 2016.

through April and May, by which point they were seen across the entire Pacific basin. These westward anomalies acted to reverse the sea level anomaly pattern across the basin (Figs. 3.16c,d) and erase the >2°C SST anomalies in the eastern tropical Pacific (see Figs. 3.2a–c). In June, these anomalies began to weaken in the eastern half of the basin, and in July, they weakened across the basin when peak anomalies of ~25 cm s⁻¹ were at 3°–4°N. These westward anomalies continued to weaken throughout the rest of the year; in December, they averaged 10–15 cm s⁻¹ at 4°–6°N.

As noted in earlier *State of the Climate* reports (e.g., Dohan et al. 2015), the Kuroshio was shifted anomalously northward in 2010–14, although this shift diminished in 2014. During 2015 and 2016, the Kuroshio was close to its climatological latitude.

Equatorial Pacific surface current anomalies advect surface waters across the basin, resulting in SST anomalies. These surface current anomalies typically lead SST anomalies by several months, with a magnitude that scales with the SST anomaly magnitude. SST anomalies typically continue to rise until the currents return to normal conditions. Thus, current anomalies in this region are a valuable predictor of the evolution of SST anomalies and their related climate impacts. This leading nature can be seen in the first principal empirical orthogonal function (EOF) of surface current anomaly (SC) and separately the first EOF of SST anomaly (SST) in the tropical Pacific basin (Fig. 3.20). The maximum lagged correlation between SC and SST is R = 0.66 for 1993–2016, with SC leading SST by 81 days. The year began with positive SST and SC anomalies. SC anomalies sharply reversed in January, dropping to a minimum EOF

amplitude value of −2.9 standard deviations in April—the smallest value in the record—and remaining negative throughout the year. These westward SC anomalies resulted in a lowering of SST anomalies, although with such strong positive SST anomalies at the start of the year, the SST EOF amplitude remained positive for most of 2016.

2) INDIAN OCEAN

The annually averaged near-equatorial current in the Indian Ocean basin is eastward, reflecting the dominance of the Southwest Monsoon Current in the annual average. During 2016, the mean current near the equator was up to 20 cm s⁻¹ faster (anomalous eastward current) in the eastern half of the basin, with the largest anomalies at 6°–8°S. Because these anomalies were not seen in 2015, they appear in both the 2016 annual average (Fig. 3.18a) and the 2016 minus 2015 tendencies (Fig. 3.18b). An examination of the month-by-month development of these anomalies reveal that they reflect a much-stronger-than-average Southwest Monsoon Current in the second half of the year. The year 2016 began with >20 cm s⁻¹ westward anomalies from 5°S to 1°N in the central Indian Ocean, which weakened in February and March and were largely absent by April. In May, very strong (25 cm s⁻¹) eastward equatorial anomalies developed across the

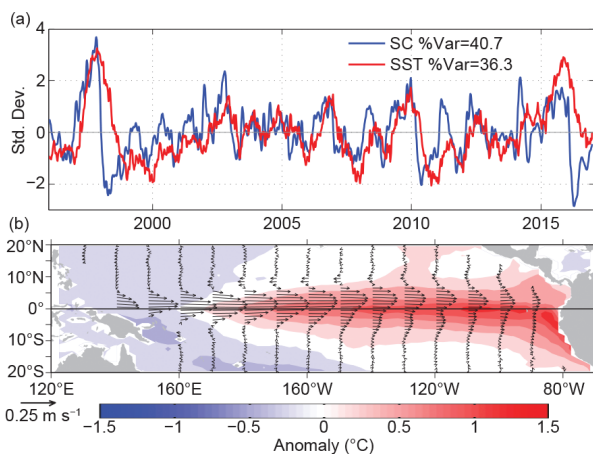**FIG. 3.20. Principal empirical orthogonal functions (EOF) of surface current (SC; m s⁻¹) and of SST anomaly (°C) variations in the tropical Pacific from the OSCAR model (Bonjean and Lagerloef 2002; www.esr.org/enso_index.html). (a) Amplitude time series of the EOFs normalized by their respective standard deviations. (b) Spatial structures of the EOFs.**

basin. Through June and July, these anomalies intensified and propagated east and south, as the current is deflected off the equator by the presence of the Malaysian coast. The anomalies weakened slightly in August, then persisted at approximately the same strength (30–35 cm s^{-1} eastward in the region 6°–8°S, 80°–100°E) through the end of 2016.

The Agulhas Current transport is a key indicator of Indian–Atlantic Ocean interbasin water exchanges. The annual mean transport of the Agulhas Current decreased over the period 2013–15, from 56 Sv (1 Sv ≡ 10^6 m^3 s^{-1}) in 2013 to 50 Sv in 2015 (www.aoml.noaa.gov/phod/altimetry/cvar). In 2016, the Agulhas Current had an annual average transport of 54 Sv, exceeding the long-term mean of 50 Sv. These changes are larger than the ~3 Sv standard deviation of the individual yearly estimates.

3) ATLANTIC OCEAN

Annual mean anomalies in the Atlantic Ocean (Fig. 3.18a) indicate an 8–10 cm s^{-1} strengthening of the eastward NECC and comparable weakening of the westward northern South Equatorial Current (nSEC) at 2°–5°N, 15°–40°W. Elsewhere, conditions were near climatology. Because anomalies were weaker in 2015, the 2016 minus 2015 map (Fig. 3.18b) closely resembles the 2016 map. Looking at the month-to-month development of anomalies, large-scale conditions were close to climatology until May, when eastward anomalies began developing across the equatorial band, indicating a slowing of the westward nSEC. By June, these anomalies exceeded 20 cm s^{-1} at 1°–3°N, 0°–30°W. They then weakened through July and August, when eastward anomalies began developing to the north, in the latitude band of the NECC. These anomalies, which dominated the annual average, intensified through September–November in the western NECC and were still present at the end of the year. Averaged over the last four months of the year, eastward anomalies peaked at 30 cm s^{-1} at 4°N, 30°–45°W. Weaker westward anomalies centered at 6°N in the same longitude band indicate that the NECC was not only stronger, but also shifted somewhat south of its climatological position.

The mean position of the Gulf Stream extension shifted north by approximately 0.5° latitude in 2016 relative to climatological values (see Sidebar 3.1 for related impacts), while the Loop Current did not extend as fully into the Gulf of Mexico on average in 2016 as it had in the previous two years.

In the southwest Atlantic Ocean, the Brazil Current carries waters from subtropical to subpolar regions mainly in the form of large anticyclonic rings

(Lentini et al. 2006). The separation of the Brazil Current front from the continental shelf break continued to exhibit annual periodicity (www.aoml.noaa.gov/phod/altimetry/cvar), which is mainly driven by wind stress curl variations and the transport of this current. During 1993–2005, the annual mean separation of the front shifted southward in response to a long-term warming in South Atlantic temperatures (cf. Lumpkin and Garzoli 2011; Goni et al. 2011). Since 2005, the location of the front has not exhibited interannual trends. The year 2016 was an anomalous one in which the front was persistently shifted north of its long-term mean position—something not seen since 1994. It remains to be seen if this represents a transient or more sustained reversal of the long-term shift of the confluence to the south.

h. Meridional overturning and oceanic heat transport circulation observations in the North Atlantic Ocean— M. O. Baringer, D. A. Smeed, J. Willis, M. Lankhorst, W. R. Hobbs, S. Dong, G. McCarthy, D. Rayner, W. E. Johns, G. Goni, and U. Send

This section describes the AMOC and the Atlantic meridional heat transport (AMHT), determined by the large-scale ocean circulation wherein northward moving upper layer waters are transformed into deep waters that return southward, redistributing heat, fresh water, carbon, and nutrients. Large variations in meridional heat transport are associated with strong MOC anomalies (e.g., correlations of 0.94, Johns et al. 2011) and northwesterly wind anomalies while monthly variability is more closely linked to the spatial structure associated with the North Atlantic oscillation (NAO; e.g., Moat et al. 2016). Observed cold North Atlantic sea surface temperatures were consistent with the decadal decrease in MOC transport at 26°N (e.g., Baringer et al. 2016). These large-scale ocean anomalies can subsequently impact European weather (e.g., Duchez et al. 2016). Many climate, weather, and ecosystem changes covary with changes in the AMOC (e.g., Srokosz and Bryden 2015; Carton et al. 2014; Srokosz et al. 2012).

The AMOC is computed as the maximum of the vertical accumulation of the horizontally integrated velocity across a zonal-vertical section (i.e., the maximum transport that occurs in either the upper or lower layer before the circulation starts to change direction again). The AMHT involves the covariability of temperature and velocity and is only meaningful as a flux (and hence, independent of the absolute temperature scale used) when the total mass transport can be accounted for (i.e., sums to zero). Observing systems can measure both temperature and velocity, usually with tradeoffs in system design

that favor the computation of one quantity over the other. Here we describe the AMOC from observing systems at 41°N, 26°N, and 16°N and AMHT at 41°N, 26°N, and 35°S.

The longest time series of ocean transport to serve as an index of the AMOC's strength in the North Atlantic (e.g., Frajka-Williams 2015; Duchez et al. 2014) is from the Florida Current (FC, as the Gulf Stream is called at 26°N), measured since 1982 (Fig. 3.21). FC and AMOC transport variations at all time scales also are inversely linked to sea level variations along the U.S. East Coast (e.g., McCarthy et al. 2015). The median 1982–2016 transport of the FC is 31.9 (±0.25) Sv, with the uncertainty being one standard error of the mean assuming a 20-day integral time scale. There is a small downward trend in the record of −0.30 (±0.24) Sv decade^{-1}, this time with 95% significance levels. The 2016 median FC transport was 31.8 (±1.9) Sv, not statistically significantly below the long-term average. Daily FC transports compared to those of all previous years (Fig. 3.21) indicate that 2016, like previous years, included several unusual transport anomalies (extremes defined as outside the 95% confidence limits for daily values). During 2016 there were two high transport events during 31 July–3 August and 10–11 September, with transport in excess of 38.8 Sv. Low transport anomalies occurred during 15–21 April, 10–23 October, and 13–15 November 2016. The lowest daily 2016 FC transport was 19.8 (±1.7) Sv on 18 April, with transports < 23 Sv for five days around this date. Of note is the coincidence of the low transport events in October and November with king tide events in South Florida, which caused widespread street flooding, and the 14 November 2016 "supermoon" (see www.nasa.gov/feature/goddard/2016/novembers-spectacular-supermoon). The difference between the observed sea level at the Lake Worth tide gauge station was larger than the predicted tidal sea level during these events (Fig. 3.21) and inversely correlated with the FC transport at well over the 99% significance level (correlation coefficient −0.62, 37% of variance explained).

In the North Atlantic, the latitudes with currently available AMOC estimates include 41°N, where a combination of profiling Argo floats (that measure ocean temperature and salinity for the upper 2000 m on broad spatial scales, as well as velocity at 1000 m) and altimetry-derived surface velocity (Willis 2010) are used to estimate the AMOC (Fig. 3.22) and AMHT (Fig. 3.23). This time series has been updated since last year's report (Baringer et al. 2016), extending from January 2002 to April 2016. At 26°N, the AMOC (Fig. 3.22) and AMHT (Fig. 3.23) are measured with

full-water column moorings that span the full basin and include direct transport measurements in the boundary currents as part of the large RAPID-MOC/MOCHA/WBTS 26°N mooring array (Smeed et al. 2015). The data from this array are collected every 18 months; hence the MOC data shown here extend from April 2004 to October 2015 (MHT data available to April 2014). At 16°N, a mooring array of inverted echo sounders, current meters, and dynamic height moorings (Send et al. 2011) measures the flow below 1000 m (the southward flowing part of the AMOC "conveyor belt") that sends North Atlantic Deep Water toward the equator; hence, the AMOC estimate at this latitude (Fig. 3.22) is a negative number (southward deep flow) to distinguish these observations from the full water column systems. Since this array only measures the deep circulation, an estimate of the AMHT is
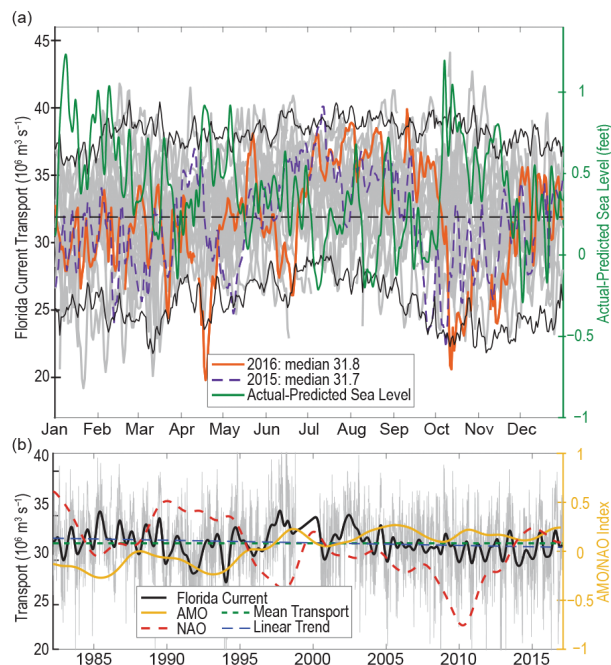

FIG. 3.21. (a) Daily estimates of Florida Current transport (10^6 m^3 s^{-1}) during 2016 (orange solid line), 2015 (dashed purple line), and 1982–2016 (light gray lines) with 95% confidence interval of daily transport values computed from all years (black solid line), the long-term mean (dashed black line), and actual observed sea level at the Lake Worth Pier tide gauge station minus predictions (green line) based on NOAA harmonic tide constituents (https://tidesandcurrents.noaa.gov/stationhome.html?id=8722670). (b) Daily estimates of Florida Current transport (10^6 m^3 s^{-1}) for the full record (light gray), smoothed using a 12-month second-order Butterworth filter (heavy black line), mean transport for the full record (dashed green line), and linear trend for 1982–2016 (dashed blue line). Two-year low-passed AMO (yellow line) and NAO (red dashed line) indices are also shown.
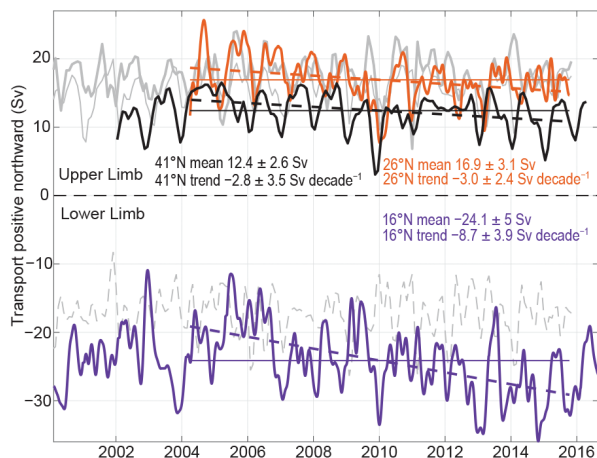
FIG. 3.22. Estimates of 2000–16 AMOC (Sv) from the Argo/Altimetry estimate at 41°N (black; Willis 2010), the RAPID-MOC/MOCHA/WBTS 26°N array (red; McCarthy et al. 2015), and the German/NOAA MOVE array at 16°N (blue; Send et al. 2011); a 3-month second-order Butterworth low-pass filter is also applied. Horizontal lines are mean transports during similar time periods as listed in the corresponding text. Dashed lines are trends for each series. For MOVE data, the net zonal and vertical integral of the deep circulation represents the lower limb of the AMOC (with a negative sign indicating southward flow), and hence a stronger negative (southward) flow represents an increase in the AMOC amplitude. Light gray lines show EC-derived transports (Menemenlis et al. 2008): (top) thin gray is the 41°N transport, thick gray is the 26°N transport, (bottom) shows the negative meridional overturning circulation in the model for ease of comparison with the 16°N data.

impossible at 16°N because of the missed large signals and high correlations in the surface waters. These data have been updated since last year's report and now extend from February 2000 to September 2016. At 35°S in the South Atlantic, the AMHT is estimated using a combination of high-density (closely spaced) expendable bathythermograph (XBT) and broader-scale Argo profiling float data (Dong et al. 2014). While the AMOC has also been estimated at 35°S, those estimates (not shown) are rough because the XBTs only extend to 750 m. These data are collected and analyzed in near-real time, with values spanning July 2002 to August 2016.

In the far North Atlantic the MOC time series continue the relatively low trend in MOC transport: the trend of the MOC at 26°N is −3.0 (±2.4) Sv decade^{-1} (Fig. 3.22) and the MHT trend is −0.23 (±0.19) PW decade^{-1} (1 PW = 10^{15} W; Fig. 3.23). At 41°N these trends are −1.2 (±3.0) Sv decade^{-1} and −0.09 (±0.21) PW decade^{-1}. These values are for the full length of each time series, while Fig. 3.22 lists

the trends for the overlapping time periods of each time series (denoted by the dashed line in each panel). These trends are not statistically significantly less than those in last year's report (−4.1 (±3.2) Sv decade^{-1} and −0.23 (±0.19) PW decade^{-1} at 26°N and −1.3 (±4.9) Sv decade^{-1} and −0.15 (±0.27) PW decade^{-1} at 41°N), despite slightly larger MOC and MHT transports reported this year (e.g., at 26°N, the mean MOC increased from 16.0 Sv in 2014 to 16.3 Sv in 2015, and at 41°N, the mean MOC increased from 10.7 Sv in 2015 to 12.5 Sv in 2016). As more data become available, the 26°N data show flow compensation between the FC and upper flows in the center of the ocean, resulting in recirculation that is not associated with a change in the MOC (Frajka-Williams et al. 2016).

Farther south, the MOC and MHT trends are positive but decreasing in the past three years as the annual means at 16°N reduced in magnitude from −29.2 Sv in 2014, to −27.8 Sv in 2015, and then to −23.8 in 2016. The trend of the AMOC from February 2000 to September 2016 at 16°N is +3.4 (±2.4) Sv decade^{-1}
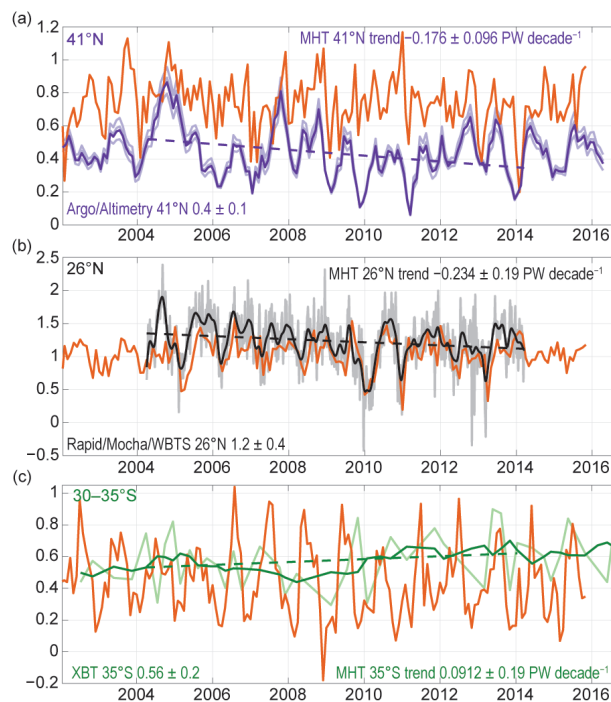

FIG. 3.23. AMHT; (PW) at (a) 41°N (from profiling floats following Hobbs and Willis 2012; blue lines), with uncertainties (light blue lines) and the trend (dashed blue line); at (b) 26°N (from mooring/hydrography data) 12-hourly values (gray line), filtered with a 3-month low-pass filter (black line), and the trend (black dashed line); and at (c) 30°–35°S (from XBTs) quarterly values (light green), filtered with yearly boxcar (dark green line), and the trend (dashed green line). Heat transports simulated by EC (orange lines; Menemenlis et al. 2008) are shown at all latitudes.

(statistically indistinguishable from the trend of +3.6 (±2.5) Sv decade^{-1} reported last year). Similarly, the 35°S AMHT transport estimate has remained fairly constant for the last three years (mean northward values of 0.60 PW in 2014, 0.69 PW in 2015, and 0.63 PW in 2016). These estimates imply a virtually steady AMOC as well (the AMOC and AMHT being highly correlated). The AMHT trend at 35°S from July 2002 to August 2016 is +0.09 (±0.10) PW decade^{-1} (again statistically indistinguishable from the trend of +0.11 (±0.10) PW decade^{-1} reported last year). Variability at all latitudes in the Atlantic is not well correlated, and therefore, data from more than one latitude are needed to describe the state of the ocean. Interannual and higher frequencies dominate the variability in the MOC and MHT time series, and therefore long records will be needed to determine decadal and longer variability.

i. *Global ocean phytoplankton*—B. A. Franz, M. J. Behrenfeld, D. A. Siegel, and S. R. Signorini

Marine phytoplankton contribute roughly half the net primary production (NPP) on Earth, fixing atmospheric CO_2 into food that fuels global ocean ecosystems and drives biogeochemical cycles (e.g., Field et al. 1998; Falkowski et al. 1998). Satellite ocean color sensors, such as SeaWiFS (McClain 2009), MODIS (Esaias et al. 1998), and VIIRS (Oudrari et al. 2015), provide observations of sufficient frequency and geographic coverage to globally monitor changes in the near-surface concentrations of the phytoplankton pigment chlorophyll-a (Chl*a*; mg m^{-3}) that serve as a proxy for phytoplankton abundance. Here, global Chl*a* distributions for 2016 are evaluated within the context of the 19-year continuous record provided through the combined observations of SeaWiFS (1997–2010), MODIS on *Aqua* (MODISA, 2002–present), and VIIRS on Suomi-NPP (2011–present). All Chl*a* data used in this analysis correspond to version R2014.0 (https://oceancolor.gsfc.nasa.gov/reprocessing), which utilized common algorithms and calibration methods to maximize consistency in the multi-mission satellite record.

The spatial distribution of VIIRS annual mean Chl*a* for 2016 (Fig. 3.24) is consistent with the well-established, physically driven distribution of nutrients (Siegel et al. 2013) and surface mixed-layer light conditions (Behrenfeld et al. 2016). To assess changes in this distribution during 2016, mean values for VIIRS Chl*a* in each month of the year were subtracted from monthly climatological means for MODISA (2003–11). These monthly fields were then averaged to produce the global chlorophyll anomaly map for 2016
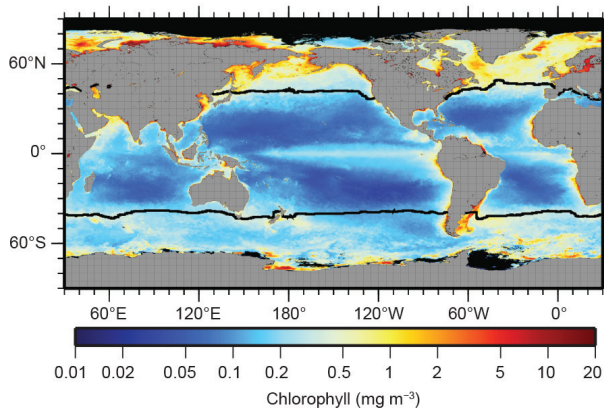

Fig. 3.24. Annual mean Chl*a* distribution (mg m^{-3}) derived from VIIRS for year 2016. Also shown is the location of the mean 15°C SST isotherm (black lines) delineating the boundary of the PSO. Chl*a* data are from NASA Reprocessing version 2014.0. Data are averaged into geo-referenced equal area bins of approximately 4.6 × 4.6 km^2 and mapped to an equirectangular projection centered at 150°W.

(Fig. 3.25a). Identical calculations were performed on MODISA sea surface temperature (SST; °C) data to produce an equivalent SST annual mean anomaly (Fig. 3.25b). The relationship between resultant annual anomalies in Chl*a* and SST are shown in Fig. 3.25c.

The dominant driver of phytoplankton Chl*a* change during 2016 was a climatic shift from El Niño to La Niña conditions. Accordingly, Chl*a* concentrations along the equatorial Pacific were elevated by 10%–20% over the climatological mean (red band in eastern equatorial Pacific in Fig. 3.25a). To the north and south of this band, Chl*a* concentrations were diminished relative to climatological values and inversely related with SST anomalies (dark blue areas above and below the equator in Fig. 3.25c). Within the boundaries of the permanently stratified ocean (PSO), delineated by the black lines in Figs. 3.24 and 3.25 at approximately 40°N and 40°S and defined as the region where annual average surface temperatures are >15°C (Behrenfeld et al. 2006), an inverse relationship was generally observed between Chl*a* and SST anomalies in the South Pacific (dark blue and dark red colors in Fig. 3.25c). By contrast, Pacific regions of the PSO north of the equator exhibited roughly an equal mix of positive and inverse relationships between Chl*a* and SST anomalies. Similarly, a mixture of Chl*a*–SST relationships was observed throughout the Atlantic and Indian sectors of the PSO. These findings for 2016 contrast with some previous findings (e.g., Behrenfeld et al. 2006, 2008, 2009; O'Malley et al. 2010; Siegel et al. 2012; Franz et al. 2013) and are further discussed below. In regions outside the PSO,
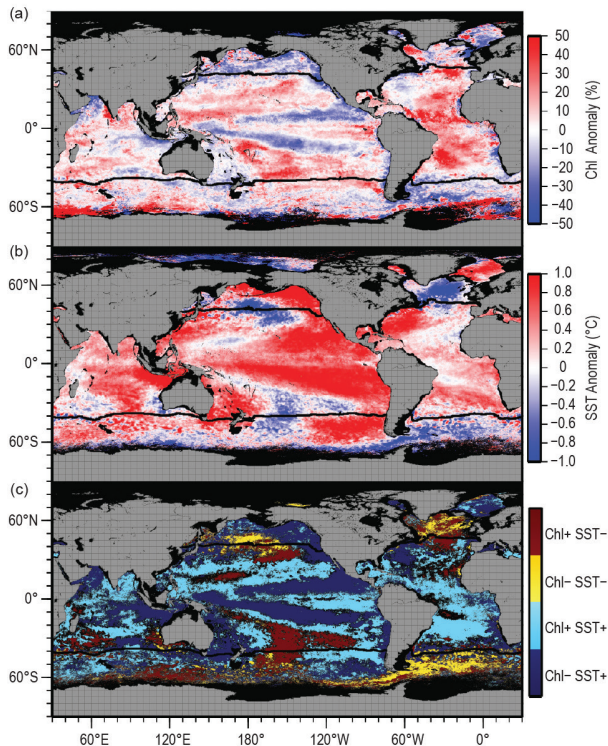
Fɪɢ. 3.25. Spatial distribution of averaged monthly 2016 (a) VIIRS Chl*a* anomalies and (b) MODISA SST anomalies, where monthly differences were derived relative to the MODISA 2003–11 climatological record. Chl*a* anomaly is expressed as % difference from climatology, while SST anomaly is shown as an absolute difference (°C). (c) identifies relationships between the sign of SST and Chl*a* anomalies from (a) and (b), with colors differentiating sign pairs and absolute changes of less than 3% in Chl*a* or 0.1°C in SST masked in black. Also shown is the location of the mean 15°C SST isotherm (black lines) delineating the PSO.

no clear relationship was observed between Chl*a* and SST anomalies (Fig. 3.25c), consistent with the previous studies cited above.

Over the 19-year time series of spatially integrated monthly mean Chl*a* values for the PSO (Fig. 3.26a), mean concentrations vary by ~20% (±0.03 mg m⁻³) around a long-term average of ~0.15 mg m⁻³ (Fig. 3.26a). This variability includes significant seasonal cycles in Chl*a* distributions and responses to climatic events. The time series also demonstrates the high level of consistency between the overlapping periods of the SeaWiFS and MODISA missions and between the MODISA and VIIRS missions, thereby lending confidence in our extension of the long-term record using measurements from VIIRS alone.

Chl*a* monthly anomalies within the PSO (Fig. 3.26b) show variations of ±15% over the multimission time series. Notable for 2016, monthly

anomalies in Chl*a* concentrations for the PSO trended consistently upward from an historical low at the start of the year (Franz et al. 2016), rising more than 20% to reach a 5% elevated state relative to the climatological reference by the end of the year. The link between these Chl*a* changes and a switch from El Niño to La Niña conditions is demonstrated as a corresponding decline in the multivariate ENSO index (MEI; Wolter and Timlin 1998; Fig. 3.26b, green diamonds, presented in the inverse to illustrate the covariation). Thus, 2016 was a transition year, which likely contributed to the weaker relationship between annual average Chl*a* and SST anomalies, as compared with similar analyses for previous years. However, monthly anomalies in PSO Chl*a* concentrations for 2016 remained consistent with the long-term ocean color record with respect to large-scale climate oscillations (Fig. 3.26b). This consistency is further evidenced in the spatial domain by comparing results shown in Fig. 3.25a with those reported by Franz et al. (2013), wherein a strikingly similar geographic distribution in Chl*a* anomalies was observed, but of opposite sign, for calendar year 2012 when the MEI was continuously trending upward.
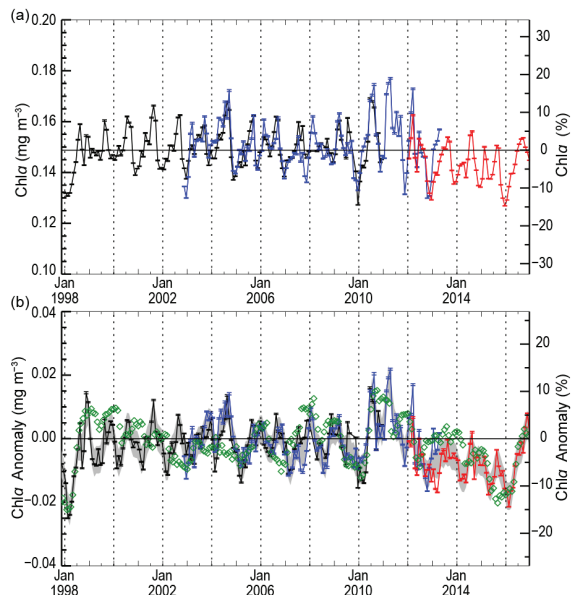

Fɪɢ. 3.26. 1998–2016, multimission record of Chl*a* averaged over the PSO for SeaWiFS (black), MODISA (blue), and VIIRS (red). (a) Independent record from each mission, with horizontal black line indicating the multimission mean Chl*a* concentration for the region (mg m⁻³). (b) Monthly anomaly (%) for SeaWiFS, MODISA, and VIIRS after subtraction of the 9-year MODISA monthly climatological mean (2003–11). The gray region in (b) shows the averaged difference between SeaWiFS and MODISA over the common mission lifetime. Green diamonds show the MEI, inverted and scaled to match the range of the Chl*a* anomalies.

Surface layer Chl*a* concentrations, as derived from ocean color remote sensing, have long functioned as a central property for monitoring global changes in marine phytoplankton. Variability and trends in Chl*a* reflect both adjustments in phytoplankton biomass and physiology (or health). Both of these properties are mechanistically linked to physical properties of the upper ocean, as well as ecological relationships between phytoplankton and their zooplankton predators. Unraveling this diversity and often covariation of factors that influence Chl*a* concentrations is essential for correctly interpreting the implications of Chl*a* anomalies for ocean biogeochemistry and food webs. For example, inverse relationships between Chl*a* and SST can emerge from changes in either mixed-layer light levels or vertical nutrient flux, but these two mechanisms have opposite implications for phytoplankton NPP (Behrenfeld et al. 2016). An additional complication is that measured changes in ocean color often reflect, at least in part, changes in colored dissolved organic matter signals (Siegel et al. 2005) that are mistakenly attributed to Chl*a* changes (Siegel et al. 2013). Thus, while the satellite record of ocean color continues to provide critical insights on global processes, new insights and approaches are needed to fully understand the story these data are telling regarding relationships between climate and marine ecosystems.

j. Global ocean carbon cycle—R. A. Feely, R. Wanninkhof, P. Landschützer, B. R. Carter, and J. A. Triñanes

The global ocean is a major sink for anthropogenic carbon dioxide (CO_2) that is released into the atmosphere from fossil fuel combustion, cement production, and land use changes. Over the last decade the global ocean has continued to take up a substantial fraction of the anthropogenic carbon (C_{anth}) emissions and is therefore a major mediator of global climate change. Of the 10.2 ($\pm$0.7) Pg C yr^{-1} C_{anth} released during the period 2006–15, about 2.6 ($\pm$0.5) Pg C yr^{-1} (26%) accumulated in the ocean, 3.1 ($\pm$0.8) Pg C yr^{-1} (30%) accumulated on land, and 4.5 ($\pm$0.1) Pg C yr^{-1} (43%) remained in the atmosphere (Global Carbon Project 2016). This decadal ocean carbon uptake estimate is a consensus view based on a combination of measured decadal inventory changes, models, and global air–sea CO_2 flux estimates based on surface ocean partial pressure of CO_2 (pCO_2) measurements. Using ocean general circulation models that include biogeochemical parameterizations (OBGCMs) and inverse models that are validated with observations-based air–sea exchange fluxes and basin-scale ocean inventories, Le Quéré et al. (2016) have demonstrated

that the oceanic anthropogenic carbon sink has grown from 1.2 ($\pm$0.5) Pg C yr^{-1} in the decade of the 1960s to 2.6 ($\pm$0.5) Pg C yr^{-1} in the decade from 2006 to 2015. Air–sea flux studies reported here indicate an ocean uptake of C_{anth} of 2.5 ($\pm$0.5) Pg C yr^{-1} for 2016, with the uncertainty being the standard deviation of monthly values.

1) Air–sea carbon dioxide fluxes

Ocean uptake of C_{anth} can be estimated from the net air–sea CO_2 flux derived from the bulk flux formula with air–sea differences in CO_2 partial pressure (ΔpCO_2) and gas transfer coefficients as input (Wanninkhof 2014). A steady contribution of carbon from continental runoff estimated at 0.45 Pg C yr^{-1} (Jacobson et al. 2007) is included to obtain the C_{anth}. The data source for pCO_2 are annual updates of surface water pCO_2 observations from the Surface Ocean CO_2 Atlas (SOCAT) composed of mooring and ship-based observations (Bakker et al. 2016). The ΔpCO_2 and a parameterization of the gas transfer with wind described in Wanninkhof (2014) are used to calculate the air–sea CO_2 fluxes. Increased observations and improved mapping techniques (e.g., Rödenbeck et al. 2015) now afford global pCO$_2$ fields at a 1° grid on monthly time scales with a lag of less than three months. This progress allows investigation of variability on subannual to decadal time scales.

The monthly 2016 ΔpCO_2 maps are based on an observation-based neural network approach (Landschützer et al. 2013, 2014) applied to biogeographical provinces. Surface temperature, sea surface salinity, climatological mixed-layer depth, satellite chlorophyll-a, and atmospheric CO_2 are used to establish relationships with surface ocean pCO_2 measurements and are applied where no observations exist. The 2016 air–sea estimate uses wind speeds from 2015 as consistent global wind products for 2016 have not been processed. Changes in winds over time have a small effect on gas transfer (Wanninkhof and Triñanes 2017) so this approximation should not have a determining impact on the interpretation of the air–sea CO_2 fluxes calculated for 2016.

The C_{anth} fluxes from 1982 to 2016 (Fig. 3.27) suggest a decreasing ocean sink in the first part of the record and a strong increase from 2001 onward. The amplitude of seasonal variability is ~1 Pg C with minimum uptake in June–September. The C_{anth} air–sea flux of 2.5 ($\pm$0.5) Pg C yr^{-1} in 2016 is 32% above the 2005–14 average of 1.9 ($\pm$0.5) Pg C yr^{-1}.

The average fluxes in 2016 (Fig. 3.28a) show the characteristic pattern of effluxes in the tropical regions, with the largest effluxes in the equatorial Pa-
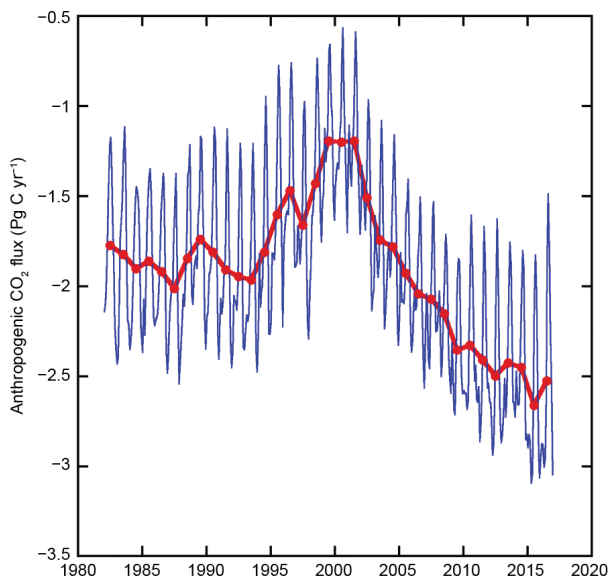
FIG. 3.27. Annual (red line) and monthly (blue line) C_{anth} fluxes (Pg C yr^{-1}) from 1982–2016. Negative values indicate uptake by the ocean.

cific and Arabian Sea upwelling regions. Large sinks are observed poleward of the subtropical fronts. The Southern Ocean is a strong sink but net annual effluxes are apparent in the Polar Front regions (55°–60°S) in the Indian and Pacific sectors of the Southern Ocean.

Ocean uptake anomalies (Fig. 3.28b) in 2016 relative to the 1995–2015 average are attributed to the increasing ocean CO_2 uptake with time and to several climate reorganizations. The air–sea flux trend since 2000 is −0.7 (±0.08) Pg C decade^{-1}, which leads to predominantly negative flux anomalies (greater uptake). Despite this strong trend there are several regions showing positive anomalies for 2016, notably the eastern equatorial, western, and North Pacific. The subtropical gyres in the North Atlantic and southern Indian Oceans show positive anomalies as well. The positive anomalies are attributed to changes in ocean circulation patterns; however, they are often difficult to attribute to a single cause. The increased effluxes in the eastern equatorial Pacific are possibly caused by the changes in ENSO patterns, with the largest impacts of the recent El Niños being farther west in the central rather than eastern equatorial Pacific (Ashok and Yamagata 2009). Stronger effluxes in the western and North Pacific are related to strongly positive PDO values in 2015–16 as well as the residual of the 2013–15 warm anomaly in the northern North Pacific (Bond et al. 2015) that persisted into the first half of 2016 (Fig. 3.28c).

The differences between the air–sea CO_2 fluxes in 2016 compared to 2015 (Fig. 3.28c) are easier to place in context of changes in temperature, circulation, and

climate reorganizations as the longer-term trends do not obfuscate the changes. The anomalously high CO_2 effluxes in the northeast Pacific associated with the anomalously warm temperatures of the 2013–15 warm anomaly have shifted northward in this region. The equatorial Pacific shows an increase in CO_2 fluxes near the equator associated with increasing upwelling after the termination of the 2015/16 El Niño. This shift is also reflected by cooler SST in the region (see Fig. 3.1). The strong increase in uptake in the Atlantic subpolar gyre in 2016 is associated with warmer SST, suggesting that less cold deep waters with high pCO_2 were entrained into the surface mixed layer. The strong positive flux anomaly near the polar front in the southeastern sector of the South Pacific Ocean is likely associated with regionally enhanced upwelling of cold deep water with high CO_2. This
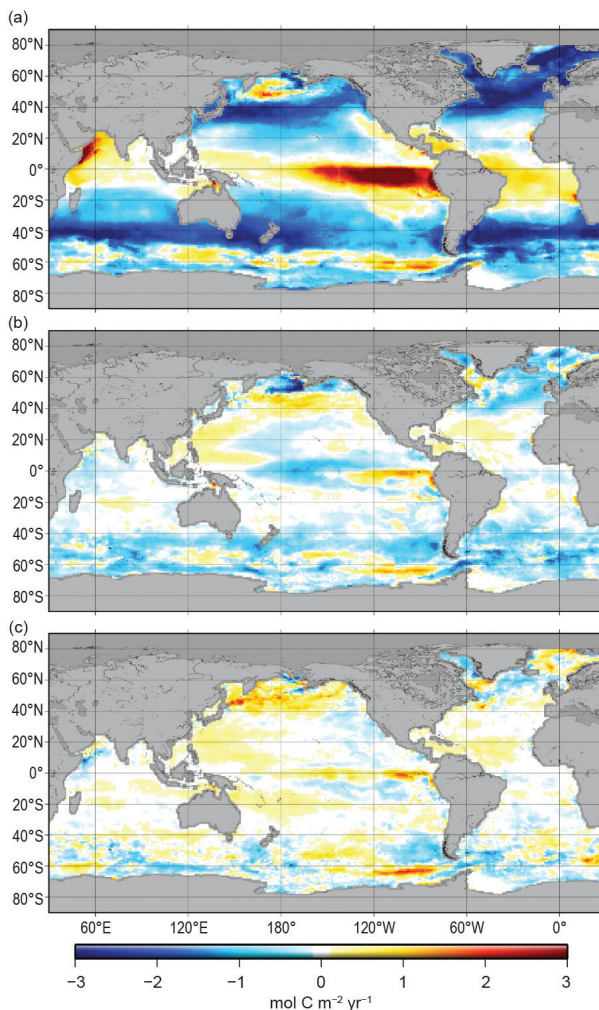

FIG. 3.28. (a) Net air–sea fluxes for 2016; (b) net air–sea flux anomalies for 2016 compared to the average for 1995–2015; and (c) net air–sea flux anomalies for 2016 compared to the 2015 values following the method of Landschützer et al. (2013). Anomalies are in mol C m^{-2} yr^{-1}.

feature has the expected small negative SST anomaly associated with it. However, the SST anomaly appears greater in the Atlantic sector and has a strong negative, rather than a positive, flux anomaly associated with it. This relation shows that, while many of the flux/pCO$_2$ anomalies can be attributed to climate reorganizations and associated physical anomalies, notably temperature, the causality is often complex. For example, the behavior of pCO$_2$ with respect to temperature includes competing processes: thermodynamics dictate decreasing pCO$_2$ with decreasing SST but waters originating from the deep with a cold temperature signal will have a high pCO$_2$.

The strong trend of increasing uptake since 2002 reached its largest uptake value in 2015 and in 2016 has decreased slightly, largely to decreased uptake in June–September (Fig. 3.27). This small decrease in global uptake is well within the envelope of interannual variability and should not be inferred as a longer-term saturation of the ocean CO$_2$ sink.

2) CARBON INVENTORIES

The U.S. Global Ocean Ship-based Hydrographic Investigations Program (GO-SHIP) is providing new information about the uptake and storage of carbon within the ocean interior by determining the change in measured dissolved inorganic carbon (DIC) concentrations and calculations of estimated C$_{anth}$ concentration changes between decadal cruise reoccupations. A recent example is the DIC concentrations (Figs. 3.29a,c,e) and the DIC differences (Figs. 3.29b,d,f) for the three P18 cruises that occurred in 2016/17, 2007/08, and 1994. The high decadal DIC differences among the P18 cruises in the Pacific show the buildup of DIC of up to 50 μmol kg^{-1} resulting from gas exchange, mixing, and transport of the water masses in the surface and intermediate waters to depths down to approximately 1500–2000 m. On these approximately decadal time scales, increases are expected in the lighter density thermocline waters found shallower than ~2000 m. These increases are owing to continued surface ocean uptake of CO$_2$, which are in turn owing to atmospheric increases caused by human activities, primarily burning of fossil fuels. Apparent noise in this increase is due to large
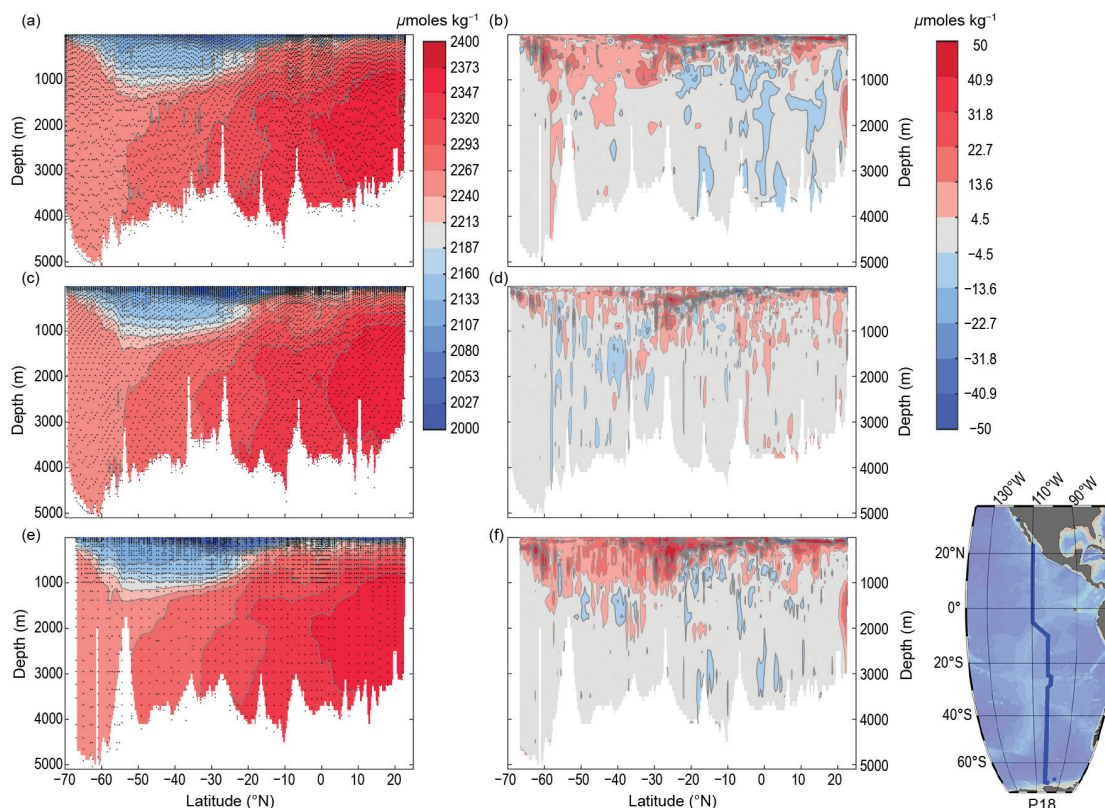

FIG. 3.29. Vertical-meridional sections of total DIC measured along the GO-SHIP P18 section in (a) 2016/17, (c) 2007/08, and (e) 1994. DIC change sections (red indicates increases) between (b) 2007/08 and 1994 cruises, (d) 2016/17 and 2007/08 cruises, and (f) 2016/17 and 1994 cruises. For this comparison, measured property values were interpolated vertically using a cubic Hermite piece-wise polynomial method and interpolated linearly against latitude onto a fixed grid.

DIC variability from changes in ocean circulation on decadal and shorter time scales. Planned future work will quantify the fraction of the observed changes that are directly attributable to increases of CO_2 from human activities. These increases are expected to propagate into deeper waters on longer time scales.

Using a modified version of the extended multiple linear regression (eMLR) method with Pacific cruise data, Carter et al. (2017) determined that the Pacific Ocean (from 60°N to 60°S) accumulated an average of 6.1 (±1.6) Pg C decade^{-1} in the decade of 1994–2004 as compared with 8.9 (±2.2) Pg C decade^{-1} during the decade of 2004–14 (Table 3.3). The eMLR approach uses linear regressions to determine the empirical relationships between properties of interest and other hydrographic properties (salinity, potential temperature, nitrate, and silicic acid) that are also affected by water mass movements but not affected by increases in C_{anth}. The difference between the regression constants from the earlier and later datasets are then used to estimate the changes in ocean carbon independent of any changes in the water mass distributions. Using a similar approach for the Atlantic, Woosley et al. (2016) showed that C_{anth} storage increased from 5.1 to 8.1 Pg C decade^{-1} over the same time intervals. These results suggest that both increases in air–sea exchange of CO_2 at the surface as well as changes in ventilation within the ocean interior contribute to increased rates of uptake in the later decade. Because of the vast area of the subtropical gyres, the majority of the C_{anth} inventory is stored in the subtropics. By contrast, upwelling regions near the equator, in the North Pacific, and in the Southern Ocean south of the Antarctic Circumpolar Current have low storage rates (Table 3.3). In these regions, upwelling of deep waters that have been isolated from the atmosphere since the preindustrial era displace the better-ventilated, higher C_{anth} intermediate depth waters. Anthropogenic carbon inventories inferred from these different approaches are consistent with each other. (Available online at www.nodc.noaa.gov/OC5/woa13.)

TABLE 3.3. Pacific decadal C_{anth} storage for the latitude bands in Pg C decade^{-1}. The "total" values include estimates for data-poor latitude bands from 60° to 67°N and 70° to 80°S, and therefore do not exactly equal the sum of all rows (after Carter et al. 2017).

Latitude Band	WOCE to CLIVAR	CLIVAR to GOSHIP
70°–60°S	†	0.65
60°–50°S	0.56	0.84
50°–40°S	0.90	0.97
40°–30°S	0.96	1.07
30°–20°S	0.65	1.31
20°–10°S	0.35	1.20
10°–0°S	0.29	0.72
0°–10°N	0.46	0.56
10°–20°N	0.79	0.52
20°–30°N	0.60	0.64
30°–40°N	0.35	0.53
40°–50°N	0.13	0.35
50°–60°N	0.07	0.21
Southern Hemisphere	3.8 ± 1.0	6.8 ± 1.7
Northern Hemisphere	2.4 ± 0.6	2.8 ± 0.7
Total (60°S–60°N)	6.1 ± 1.6	8.9 ± 2.2
† insufficient data		